# Tryptophan stress activates EGFR-RAS-signaling to MTORC1 and p38/MAPK to sustain translation and AHR-dependent autophagy

Pauline Pfänder[1,2*], Lucas Hensen[3*], Patricia Razquin Navas[3*], Marie Solvay[4,5*], Mirja Tamara Prentzell[1,2*], Ahmed Sadik[1], Alexander M. Heberle[3], Sophie Seifert[1,2], Leon Regin[6], Tobias Bausbacher[7,8], Anna-Sophia Egger[3], Madlen Hotze[3], Tobias Kipura[3], Bianca Berdel[1], Ivana Karabogdan[1,2], Luis F. Somarribas Patterson[1,2], Michele Reil[1], Deepak Sayeeram[1,2], Vera Peters[1,2], Jose Ramos Pittol[3], Ineke van ˈt Land-Kuper[9,10], Teresa Börding[6], Saskia Trump[11], Alienke van Pijkeren[3], Yang Zhang[3], Fabricio Loayza-Puch[12], Alexander Kowar[2,12], Sönke Harder[13], Lorenz Waltl[14], André Gollowitzer[14], Tetsushi Kataura[15], Viktor I. Korolchuk[15], Shad A. Mohammed[7,8], Phillipp Sievers[16], Felix Sahm[16], Hartmut Schlüter[13], Andreas Koeberle[14], Carsten Hopf[7,8,17], Marcel Kwiatkowski[3], Christine Sers[6,18], Benoit J. Van den Eynde[4,5,19,20#], Christiane A. Opitz[1,21#,§], Kathrin Thedieck[3,9,10#,§]

[*, #] Equal contributions, [§]Correspondence: c.opitz@dkfz-heidelberg.de; Kathrin.Thedieck@uibk.ac.at

1 DKTK Metabolic Crosstalk in Cancer, German Consortium of Translational Cancer Research (DKTK), German Cancer Research Center (DKFZ), Heidelberg, Germany, 69120 Heidelberg, Germany.

2 Faculty of Bioscience, Heidelberg University, 69120 Heidelberg, Germany.

3 Institute of Biochemistry and Center for Molecular Biosciences Innsbruck, University of Innsbruck, 6020 Innsbruck, Austria.

4 Ludwig Institute for Cancer Research, 1200 Brussels, Belgium.

5 De Duve Institute, UCLouvain, 1200 Brussels, Belgium.

6 Laboratory of Molecular Tumor Pathology, Institute of Pathology, Charité Universitätsmedizin Berlin, 10117 Berlin, Germany.

7 Center for Mass Spectrometry and Optical Spectroscopy (CeMOS), Mannheim University of Applied Sciences, 68163 Mannheim, Germany.

8 Mannheim Center for Translational Neuroscience (MCTN), Medical Faculty Mannheim, Heidelberg University, 68167 Mannheim, Germany.

9 Department of Pediatrics, University of Groningen, University Medical Center Groningen, 9700 RB Groningen, The Netherlands.

10 Department of Neuroscience, School of Medicine and Health Sciences, Carl von Ossietzky University Oldenburg, 26129 Oldenburg, Germany.

11 Molecular Epidemiology Unite, Berlin Institute of Health at Charité Universitätsmedizin Berlin, 10117 Berlin, Germany.

12 Translational Control and Metabolism, German Cancer Research Center (DKFZ), Heidelberg, Germany, 69120 Heidelberg, Germany.

13 Institute of Clinical Chemistry and Laboratory Medicine, Section Mass Spectrometry and Proteomics, University Medical Center Hamburg-Eppendorf, 20246 Hamburg, Germany.

14 Michael Popp Institute and Center for Molecular Biosciences Innsbruck (CMBI), University of Innsbruck, 6020 Innsbruck, Austria.

15 Biosciences Institute, Faculty of Medical Sciences, Campus for Ageing and Vitality, Newcastle University, Newcastle upon Tyne, NE4 5PL, UK.

16 Department of Neuropathology, Institute of Pathology, Heidelberg University Hospital, and Clinical Cooperation Unit Neuropathology, German Consortium for Translational Cancer Research (DKTK), German Cancer Research Center (DKFZ), 69120 Heidelberg, Germany.

17 Medical Faculty, Heidelberg University, 69117 Heidelberg, Germany.

18 German Cancer Consortium (DKTK), Partner Site Berlin, Germany.

19 Ludwig Institute for Cancer Research, Nuffield Department of Clinical Medicine, University of Oxford, OX3 7DQ Oxford, United Kingdom.

20 Walloon Excellence in Life Sciences and Biotechnology, 1200 Brussels, Belgium.

21 Neurology Clinic and National Center for Tumor Diseases, 69120 Heidelberg, Germany.

## SUMMARY

Limited supply and catabolism restrict the essential amino acid tryptophan (Trp) in tumors. How tumors sustain translation under Trp stress remains unclear. Unlike other amino acids, Trp stress activates the EGFR, which enhances macropinocytosis and RAS signaling to the MTORC1 and p38/MAPK kinases, sustaining translation. The AHR forms part of the Trp stress proteome and promotes autophagy to sustain Trp levels, and ceramide biosynthesis. Thus, Trp restriction elicits pro-translation signals enabling adaptation to nutrient stress, placing Trp into a unique position in the amino acid-mediated stress response. Our findings challenge the current perception that Trp restriction inhibits MTORC1 and the AHR and explain how both cancer drivers remain active. A glioblastoma patient subgroup with enhanced MTORC1 and AHR displays an autophagy signature, highlighting the clinical relevance of MTORC1-AHR crosstalk. Regions of high Trp or high ceramides are mutually exclusive, supporting that low Trp activates the EGFR-MTORC1-AHR axis in glioblastoma tissue.

## HIGHLIGHTS

- Under Trp stress,
  - EGFR-RAS signaling activates macropinocytosis, MTORC1 and p38.
  - MTORC1 and p38 driven translation induces AHR levels and activity.
  - AHR enhances ceramides and autophagy, sustaining intracellular Trp.
- In glioblastoma, ceramides localize to low Trp areas, and high AHR associates with MTORC1 activity and autophagy.

## KEYWORDS

tryptophan (Trp) stress; EGF receptor (EGFR); RAS GTPase; mTOR complex 1 (MTORC1); 4E binding protein 1 (4E-BP1, EIF4EBP1); p38; mitogen-activated kinase (MAPK); aryl hydrocarbon receptor (AHR); protein biosynthesis; macropinocytosis; lysosomes; autophagy; ceramides

## INTRODUCTION

Protein biosynthesis is essential for tumor survival and progression (Fabbri et al., 2021; Kovalski et al., 2022) and requires an adequate supply of amino acids. Cancers contain poorly vascularized areas and tumor blood vessels are dilated and leaky, collectively compromising nutrient delivery to tumor cells. As the least abundant essential amino acid (Barik, 2020; Klaessens et al., 2022), tryptophan (Trp) will be the first amino acid to become limiting upon nutrient restriction in tumors. In addition, Trp catabolism is often upregulated in tumors and activation of the aryl hydrocarbon receptor (AHR) by Trp catabolites promotes tumor progression (Gargaro et al., 2021). Glioblastoma are paradigmatic of such a situation: via the AHR, Trp catabolites promote glioblastoma progression (Gabriely et al., 2017; Platten et al., 2021). Trp levels decline with increasing distance from blood vessels in a glioblastoma model (Kumar et al., 2019), glioblastoma patients exhibit decreased blood Trp levels (Opitz et al., 2011; Panitz et al., 2021; Zhai et al., 2015), and human glioblastoma tissues show areas of low Trp (Panitz et al., 2021). However, the mechanisms via which the tumors sustain translation under Trp stress are poorly understood. We showed previously that Trp depletion increases the levels of the tryptophanyl-tRNA-synthetase (WARS), channelling the remaining Trp molecules into translation (Adam et al., 2018). This explains how peptide elongation at Trp codons is enabled under low Trp conditions. Yet, also translation initiation is tightly coupled to amino acid sufficiency and is suppressed as amino acid levels drop (Fabbri et al., 2021; Kovalski et al., 2022). In keeping with this, Trp stress elicits signaling events which block translation initiation: Trp depletion leads to an increase in uncharged tryptophanyl tRNA which activates the EIF2A kinase GCN2 (general control non-derepressible 2, encoded by EIF2AK4) (Munn et al., 2005). GCN2 represses cap-dependent translation initiation by phosphorylating the eukaryotic translation initiation factor 2 alpha (EIF2A) at serine 51 (Roux and Topisirovic, 2018). Upon amino acid sufficiency, the MTOR complex 1 (MTORC1) kinase enhances translation initiation. The RAG GTPases recruit MTORC1 to the lysosomal surface where it is activated further by RHEB (Ras homolog enriched in brain) GTPase downstream of the TSC (tuberous sclerosis complex) protein complex that integrates growth factor signals coming from AKT and MAPK (mitogen activated protein kinase) signaling (Alesi and Henske, 2022; Battaglioni et al., 2022; Fumagalli and Pende, 2022; Inoki and Guan, 2022; Valvezan and Manning, 2019). Withdrawal of amino acids, including arginine, leucine, methionine, glutamine and asparagine, is known to inactivate MTORC1 through inhibition of the RAG GTPases (Deleyto-Seldas and Efeyan, 2021) and other lysosomal regulators (Hesketh et al., 2020; Melick and Jewell, 2020; Meng et al., 2020). Relatively little is known about Trp stress signals to MTORC1. Two studies showed that Trp deprivation inhibits phosphorylation of the *bona fide* MTORC1 substrate S6K (RPS6KB1) at T389 (Fiore et al., 2022; Metz et al., 2012), which is in line with the idea that

MTORC1 activity is low and does not activate translation. Another translation initiation signal is transduced by the MAPK pathway through MNK1 (MKNK1) which directly phosphorylates and enhances the activity of the translation initiation factor EIF4E, specifically in the context of cancer (Roux and Topisirovic, 2018). Whether and how Trp restriction impinges on this pathway is unknown. Thus, we do not yet know how tumor cells sustain translation, needed for tumor progression under Trp stress.

We report that Trp restriction activates EGFR and RAS signaling towards the MTORC1 and MKNK1 kinases. They sustain translation initiation by inhibiting the EIF4E repressor 4E-binding protein 1 (4E-BP1, EIF4EBP1) and by directly phosphorylating EIF4E, respectively. The Trp stress proteome features enhanced AHR expression and exhibits enrichment of macropinosome and lysosomal proteins. MTORC1-driven AHR activity promotes autophagy, thus fueling the cells with Trp, and increasing ceramide levels. We hence identify the EGFR-RAS axis as a key element of the Trp stress response. Our findings challenge the current perceptions that Trp stress (1) inhibits MTORC1 due to lack of an essential amino acid (Metz et al., 2012), and (2) represses the AHR due to the absence of Trp-derived ligands. We find in human glioblastoma that MTORC1 activity and autophagy associate with increased AHR levels. As the AHR enhances ceramide levels under Trp stress, a low Trp / ceramide ratio may identify tumors with a hyperactive EGFR.

## RESULTS

### Under Trp stress, the PI3K-MTORC1 pathway drives EIF4EBP1 phosphorylation.

We detected extensive regions of Trp restriction in human glioblastoma tissues by MALDI-MS imaging (**Figure 1A**), and wondered whether and how this aggressive tumor sustains protein biosynthesis when Trp is scarce. We conducted puromycin incorporation assays to assess *de novo* translation in LN-18 glioblastoma cells (**Figure 1B and 1C**). Physiological Trp levels of 78 µM (Psychogios et al., 2011) were compared to 24 h of Trp starvation, without and with EGF (epidermal growth factor) stimulation to enhance translation (Golan-Lavi et al., 2017)**.** Trp restriction reduced puromycin incorporation in cells without and with EGF stimulation, showing that Trp stress represses translation. Yet, the translation elongation inhibitor cycloheximide (CHX) (Ennis and Lubin, 1964) further reduced puromycin incorporation, indicating that under Trp stress translation is sustained at a lower level. Declining Trp levels enhanced the inhibitory

phosphorylation of the translation initiation factor EIF2A at S51 (EIF2A-pS51) (Adam et al., 2018; Metz et al., 2012) in a concentration dependent manner (**Figure 1D and 1E**). The level of the translation repressor EIF4EBP1 was increased (Musa et al., 2016) (**Figure 1D and 1F**), and phosphorylation of the MTORC1 substrate and translation-promoting kinase RPS6KB1 (Roux and Topisirovic, 2018) at T389 was reduced (**Figure 1D and 1G**), as reported previously (Fiore et al., 2022; Metz et al., 2012). These findings are in line with overall reduced translation. We asked which mechanisms drive protein synthesis when Trp is scarce. Of note, EIF4EBP1 phosphorylation at T37/46 was induced with decreasing Trp levels (**Figure 1D and 1H).** Upon separation by SDS-PAGE, EIF4EBP1 runs in three discernible bands (alpha, beta, gamma), all of which can be phosphorylated at T37/46 by MTORC1 (Gingras et al., 1998; Velasquez et al., 2016). We therefore quantified across all EIF4EBP1-pT37/46 signals. EIF4EBP1-T37/46 phosphorylation by MTORC1 inhibits EIF4EBP1 binding to the translation initiation factor EIF4E, thereby enhancing translation and cell growth (Schalm et al., 2003). Hence, T37/46 phosphorylation may counteract increased EIF4EBP1 expression and keep translation active under Trp stress. Furthermore, EIF4E phosphorylation at S209 was enhanced with declining Trp levels (**Figure 1D and 1I**). This MKNK1-driven event positively regulates translation in cancer (Konicek et al., 2011; Yoshizawa et al., 2010) and may hence contribute to maintain translation under Trp stress. We corroborated the results in another glioblastoma cell line. Also Trp starved LN-229 glioblastoma cells exhibited enhanced phosphorylation of both EIF4EBP1-T37/46 and EIF4E-S209 (**Figure 1J - 1L**) whereas RPS6KB1-pT389 was reduced (**Figure 1J and 1M**). The findings suggest that phosphorylation of EIF4EBP1-T37/46 and EIF4E-S209 maintain translation under Trp restriction. It was striking that Trp stress oppositely regulated the phosphorylation of the two *bona fide* MTORC1 substrates RPS6KB1 and EIF4EBP1. Apart from MTORC1, EIF4EBP1-T37/46 is phosphorylated by several other kinases (Roux and Topisirovic, 2018). We inhibited MTORC1 to test whether it mediates Trp stress induced EIF4EBP1 phosphorylation. We opted for an ATP-analogue MTOR inhibitor, which efficiently blocks phosphorylation of T37/46 in EIF4EBP1, whereas the allosteric MTORC1 inhibitor rapamycin does not (Bohm et al., 2021; Gingras et al., 1999; Gingras et al., 2001). The ATP-analogue MTOR inhibitor AZD8055 (Chresta et al., 2010) reduced Trp stress induced EIF4EBP1-T37/46 phosphorylation, demonstrating that MTOR kinase phosphorylates EIF4EBP1 when Trp is scarce (**Figure 1N – 1Q**). Trp restriction also enhanced phosphorylation of EIF4EBP1-T70, another MTORC1 substrate site (Bohm et al., 2021), in an AZD8055-sensitive manner (**Figure 1P and 1R**). Thus, MTOR phosphorylates EIF4EBP1 upon Trp stress, and the divergence of RPS6KB1 and EIF4EBP1 phosphorylation cannot be explained by distinct kinases acting on EIF4EBP1. The difference in MTORC1 affinity toward RPS6KB1 versus EIF4EBP1 (Kang et al., 2013) and a possibly different sensitivity to MTORC1 suppressors

(discussed below) may have a role in differential RPS6KB1 and EIF4EBP1 phosphorylation under Trp stress. We conclude that MTORC1 is active under Trp starvation, which expands the common view that MTORC1 is inhibited by amino acid deprivation (Fernandes and Demetriades, 2021; Liu and Sabatini, 2020; Rabanal-Ruiz et al., 2017; Valvezan and Manning, 2019) and puts Trp into a unique position in the control of MTORC1. Under nutrient sufficiency, MTORC1 is activated by class I phosphoinositide-3-kinases (PIK3CA) (Valvezan and Manning, 2019). The class I-PIK3CA inhibitor GDC-0941 (Folkes et al., 2008) inhibited EIF4EBP1-pT37/46 in Trp-restricted cells (**Figure 1S and 1T**), indicating that PIK3CA enhances MTORC1 activity towards EIF4EBP1 when Trp is scarce.

**p38 enhances EIF4E phosphorylation in Trp-deprived cells.**

We next determined the cues that mediate enhanced EIF4E-S209 phosphorylation under Trp stress. EIF4E-S209 is phosphorylated by MKNK1 (MNK1), which has been linked to activation by the MAP2K1/2 (MEK1/2) and MAPK1/3 kinases (ERK1/3) as well as to p38 (Fukunaga and Hunter, 1997; Waskiewicz et al., 1997). Trp starvation did not affect phosphorylation of MAPK1/3-pT202/Y204 (**Figure 2A and 2B**), indicating that Trp stress signals are not transduced by MEK-ERK. In agreement, the MAP2K1/2 inhibitor AZD6244 (Yeh et al., 2007) which blunted MAPK1/3-pT202/Y204, did not reduce EIF4E-pS209 in Trp deprived cells (**Figure 2A and 2C**). We tested if the p38α/β inhibitor LY2228820 (Tate et al., 2013) suppresses Trp stress induced EIF4E-S209 phosphorylation (**Figure 2D – 2F)**. In support of a p38 response to Trp stress, phosphorylation of the p38 substrate MAPKAPK2 at T334 (Rouse et al., 1994) was enhanced by Trp deprivation. LY2228820 inhibited MAPKAPK2-pT334 and partially reduced Trp-starvation-induced EIF4E-pS209, supporting that p38 contributes to EIF4E-pS209 induction by Trp stress.

**RAS and the EGF receptor are required to signal Trp stress to EIF4EBP1 and EIF4E.**

The small GTPase RAS acts upstream of PIK3CA-MTORC1 signaling and is widely accepted to be activated by growth factors (Klomp et al., 2021; Roberts and Der, 2007). RAS activation by stress (Deora et al., 1998; Grabocka and Bar-Sagi, 2016; Heberle et al., 2019; Norman et al., 2004) and RAS signaling to p38 (Lee et al., 2020; Li et al., 2000; Norman et al., 2004) is less established. Nutrient stress or Trp restriction have so far not been linked to RAS. Trp stress enhanced the levels of RAS (**Figure 2G and 2H)**, and we tested if RAS mediates Trp stress signaling towards EIF4EBP1 and EIF4E. Knockdown of all RAS isoforms (KRAS/HRAS/NRAS) reduced EIF4EBP1-pT37/46 and EIF4E-pS209 in Trp-deprived cells (**Figure 2G – 2J)**, indicating that RAS activates MTORC1 and p38 signaling. We measured RAS activity by a GST-coupled

RAF-RAS–binding domain (GST-RAFBD) pull down assay (Heberle et al., 2019), detecting GTP-bound RAS (**Fig 2K and 2L**). Trp restriction enhanced RAS binding to GST-RAFBD, indicative of enhanced GTP loading and activity of RAS.

The EGF receptor (EGFR) acts upstream of RAS (Martinelli et al., 2017) but it is unknown whether the EGFR is activated by Trp restriction. Autophosphorylation of the EGFR at Y1068 (Guntaka et al., 2011; Tang et al., 2018) was enhanced in EGF-stimulated, Trp-deprived cells (**Figure 3A and 3B).** Also without EGF stimulation, EGFR-pY1068 was induced by declining Trp levels (**Figure 3C and 3D)**. Consistent with EGFR activation (Baumdick et al., 2015), Trp stress enhanced EGFR internalization to perinuclear endosomes (**Figure 3E and 3F)**. The pan-ERBB receptor inhibitor Afatinib (Dungo and Keating, 2013) reduced Trp restriction-induced EIF4EBP1-pT37/46 and EIF4E-pS209 (**Figure 3G - 3I)**, showing that the EGFR mediates Trp stress signaling to EIF4EBP1 and EIF4E. EGFR activation by Trp restriction occurred also without exogenous EGF addition (**Figure 3C – 3F)**, suggesting a contribution by an endogenous ligand. Whereas *EGF* mRNA levels were reduced by Trp restriction (**Figure 3J**), levels of *EREG* (epiregulin) mRNA were increased (**Figure 3K**). Trp starvation also enhanced unglycosylated and glycosylated pro-EREG protein (Riese and Cullum, 2014) in a concentration-dependent manner (**Figure 3L – 3N**). EREG binds and activates all ERBB receptors (Riese and Cullum, 2014) and we asked whether the EGFR specifically mediates Trp stress signaling to EIF4EBP1 and EIF4E. Not only Afatinib but also the EGFR-specific inhibitor Erlotinib (Shepherd et al., 2005) reduced EIF4EBP1-pT37/46 and EIF4E-pS209 induction by Trp stress (**Figure 3O – 3R**). We conclude that the EGFR and RAS drive signaling to p38-EIF4E and MTORC1-EIF4EBP1 in Trp deprived cells.

**The MTORC1-EIF4EBP1 and p38-MKNK1 axes enhance translation of the AHR under Trp stress.**

Which translation events are driven by p38-EIF4E and MTORC1-EIF4EBP1 in response to Trp stress? The small compound 4EGI-1 is an EIF4EBP1 agonist that enhances EIF4EBP1-EIF4E binding and suppresses EIF4E-EIF4G association, thus inhibiting translation initiation at the cap (Moerke et al., 2007; Sekiyama et al., 2015). In Trp-deprived cells, 4EGI-1 inhibited translation to the same extent as the translation elongation inhibitor cycloheximide (**Figure 4A and 4B**), indicating that the MTORC1-EIF4EBP1 axis sustains translation under Trp stress. In agreement, MTOR inhibition by AZD8055 reduced translation in Trp starved cells (**Figure 4C – 4E**). We went on to explore the protein repertoire, which is induced when Trp is scarce. Using a label-free quantitative proteomic approach, we identified 435 proteins whose levels are increased upon Trp

restriction (**Figure 4F**). Trp limitation enhanced the enrichment of gene ontology (GO) terms related to aminoacyl-tRNA ligase activity (**Figure 4G)**, including the tryptophanyl-tRNA-synthetase WARS. This is in agreement with our earlier finding that increased WARS levels help cells to adapt to low Trp conditions (Adam et al., 2018). GO terms related to macropinocytosis and lysosomes were enriched, too (**Figure 4G**). Intriguingly, the proteome data identified the aryl hydrocarbon receptor (AHR) to be enhanced by Trp restriction **(Figure 4F)**. We confirmed the result in a Trp concentration row which showed that the AHR levels increased with declining Trp concentrations (**Figure 4H and 4I**). We investigated if this event is controlled by MTOR-driven translation downstream of the EGFR. Ribosome profiling showed an increased association of ribosomes with AHR transcripts, indicating that AHR translation is enhanced in Trp-restricted cells (**Figure 4J**). The pan-ERBB inhibitor Afatinib (**Figure 4K - 4N**), the MTOR inhibitor AZD8055 (**Figure 4O – 4Q**), the EIF4EBP1 agonist 4EGI-1 (**Figure 4R and 4S**) and the translation elongation inhibitor cycloheximide (**Figure 4T and 4U**) all suppressed AHR induction by Trp stress. We conclude that the MTORC1-EIF4EBP1-translation axis is required to enhance AHR levels under Trp starvation.

Also LY2228820 suppressed AHR levels, showing that p38 is required for AHR expression, too (**Figure 5A and 5B**). LY2228820 inhibited EIF4E-S209 phosphorylation (**Figure 2D, 2F and 5A, 5C**), which is mediated by MKNK1. In agreement, the MKNK1 inhibitor CGP-57380 inhibited Trp stress induced EIF4E-S209, but it did not affect puromycin incorporation (**Figure 5D – 5F**), showing that p38-MKNK1-EIF4E signaling does not control overall translation under Trp stress. The p38-MKNK1-EIF4E axis has been proposed to selectively enhance translation of the stress-related activating transcription factor 4 (ATF4) upon selenite restriction (Jiang et al., 2013). As ATF4 also has a major role in the response to amino acid stress (Kilberg et al., 2009), we tested whether ATF4 mediates p38 outputs when Trp is scarce. Ribosome profiling showed that ATF4 translation is enhanced in Trp-deprived cells **(Figure 5G)**. In line, Trp limitation enhanced ATF4 levels, which were suppressed by p38 inhibition (**Figure 5H and 5I**). This suggests that the p38-EIF4E axis mediates ATF4 expression in response to low Trp. An ATF4 binding motif can be found upstream of the AHR transcription start site (chr7: 173338103 – 17338111) in a region of active chromatin, supporting that ATF4 can enhance AHR expression (**Figure 5J**). In agreement, ATF4 knockdown inhibited Trp stress induced AHR levels (**Figure 5K – 5M**). Recent studies demonstrated that MTORC1 enhances ATF4 levels under insulin and nutrient sufficiency (Ben-Sahra et al., 2016; Torrence et al., 2021). We wondered whether MTORC1-driven translation impinges on ATF4 levels under Trp stress**.** AZD8055 partially reduced ATF4 levels (**Figure 5N and 5O**), suggesting that MTORC1 contributes to ATF4 induction by Trp limitation. Afatinib reduced ATF4 levels in Trp restricted cells (**Figure 5P and 5Q**), supporting that the EGFR,

upstream of p38 and MTORC1, drives ATF4 induction by Trp stress. Knockdown of EIF2AK4 (GCN2) – commonly involved in ATF4 induction by amino acid stress (Kilberg et al., 2009) – did not affect the levels of ATF4 and the AHR under Trp restriction (**Figure 5R – 5U**). Taken together, Trp stress activates the EGFR upstream of MTORC1 and p38, which enhance translation of the AHR.

**The AHR enhances autophagy to replenish intracellular Trp.**

Trp limitation not only enhanced AHR levels but also AHR activity, as determined by induction of the AHR target gene *CYP1B1* in LN-18 and LN-229 cells (**Figure 6A and 6B**). Also, RNAseq analysis revealed that Trp stress enhanced a transcriptional AHR activity signature (Sadik et al., 2020) in both cell lines (**Figure 6C and 6D**). This finding was unexpected as the AHR is typically considered to be activated by Trp metabolites (Gargaro et al., 2021; Hubbard et al., 2015; Opitz et al., 2020; Rothhammer and Quintana, 2019; Shinde and McGaha, 2018), but not under Trp restriction when Trp metabolites are low or absent. We went on to investigate the functions of the AHR upon Trp limitation. GO term analysis of the Trp-restricted proteome (**Figure 4G**) had shown enrichment of proteins related to macropinocytosis, a non-selective process driven by the EGFR and RAS (Lee et al., 2019; Nakase et al., 2015), leading to uptake of the extracellular fluid-phase and macromolecules (Puccini et al., 2022). Nutrient limitation enhances macropinocytosis, but the underlying mechanism is poorly explored (Lee and Commisso, 2020; Lee et al., 2019). We measured internalization of fluorescently-labeled dextran to stain macropinosomes and found them increased upon Trp depletion (**Figure 6E and 6F**). Upon macropinosome maturation, their content is delivered to the lysosomal compartment for degradation (Puccini et al., 2022). In agreement, lysosomal components were enriched in the GO term analysis of the Trp stress proteome (**Figure 4G**). Also the LAMP2 positive lysosomal area (**Figure 6G and 6H**) and lysosome activity (**Figure 6I and 6J**) were enhanced in Trp-restricted cells. Autophagy constitutes a lysosome function, which is critical in conjunction with macropinocytosis to break down macromolecules and fuel cancer metabolism under nutrient limitation (Puccini et al., 2022). The lipidated ubiquitin-like (Ubl) protein MAP1LC3B-II (LC3-II) decorates autophagolysosomes and serves as an anchor for autophagy receptor proteins (Dikic, 2017). To assess autophagic flux (Klionsky et al., 2021), LC3-II was detected in conjunction with inhibition of lysosome-mediated proteolysis by Bafilomycin $A_1$ (BafA) (**Figure 6K and 6L**). Under Trp sufficiency, BafA only slightly increased LC3-II, indicative of a low autophagic flux, and AHR inhibition by SR1 did not affect LC3-II levels. Trp-deprived cells exhibited higher autophagic flux, based on LC3-II induction by BafA and an increased autophagy mRNA signature (Bordi et al., 2021) (**Figure 6K – 6O**). AHR

inhibition in Trp-restricted cells reversed the LC3-II level back to that without BafA (**Figure 6K and 6L**). We conclude that the AHR promotes autophagy upon Trp restriction. Trp-starved cells exhibited a further drop in intracellular Trp when treated with BafA (**Figure 6P),** indicating that lysosomes sustain intracellular Trp levels upon Trp restriction. This finding suggests that protein scavenging by EGFR-driven macropinocytosis and subsequent AHR-mediated autophagic degradation helps glioblastoma cells to overcome Trp limitation by replenishing intracellular Trp pools.

**Glioblastoma exhibit an induced MTOR-EIF4EBP1-AHR axis, enhanced autophagy regulators and mutually exclusive areas of Trp and ceramides.**

We next interrogated whether the mechanisms we identified in cell culture are present *in vivo* in human glioblastomas. We clustered transcriptome data of human glioblastomas (The Cancer Genome Atlas, TCGA) (Colaprico et al., 2016) using the genes regulated by Trp restriction that we obtained from the RNAseq analysis of our cell culture experiments. Analysis of the clusters using the AHR activity signature identified two clusters with high AHR activity score but divergent AHR levels (**Figure 7A and 7B**, groups 1 and 2). The reverse phase protein array (RPPA) data of these clusters revealed that the cluster with high AHR levels exhibited higher EIF4EBP1-pT37/46 than the cluster with low AHR level **(Figure 7C**), whereas RPS6KB1-pT389 was similar in both patient groups **(Figure 7D**). In line with our cell culture data, this subgroup also showed enhanced expression of the transcriptional autophagy regulator signature (Bordi et al., 2021) (**Figure 7E**). Taken together, the data suggest that in a subgroup of human glioblastomas an induced MTORC1-EIF4EBP1 axis enhances AHR levels and AHR activity as well as autophagy.

Further, we investigated ceramides as a potential metabolite biomarker of AHR activity, detectable *in situ* in human tumors. The AHR positively regulates various enzymes of the ceramide biosynthetic pathway, including sphingomyelin phosphodiesterases (SMPD, sphingomyelinases) (Kennedy et al., 2013; Liu et al., 2021) that catalyze the conversion of sphingomyelin to ceramides in lysosomes (Ogretmen, 2018). The Trp restriction proteome in glioblastoma cells featured a 7-fold increase in SMPD. In agreement, Trp restriction increased the proportion of ceramides, and they were suppressed by AHR inhibition (**Figure 7F**), supporting that the AHR enhances ceramide accumulation in Trp-restricted cells. In human glioblastoma, MALDI-MS imaging revealed that the regions of high Trp and high ceramides are mutually exclusive (**Figure 7G**). To conclude, the EGFR-MTORC1-AHR axis enables tumors to overcome Trp limitation by enhancing lysosomal

activity. Tumors with large regions of low Trp and high ceramide levels may therefore be sensitive to inhibitors of EGFR, PIK3CA, MTORC1, p38, AHR, autophagy and ceramide synthesis.

## DISCUSSION

In glioblastoma, SMPD1-derived ceramides have recently been shown to activate the EGFR by modulating plasma membrane dynamics, and SMPD1 inhibition improves patient survival (Bi et al., 2021). In conjunction with our findings, this mechanism suggests a positive feedback from AHR-driven ceramide synthesis to the EGFR, further enhancing the MTORC1-AHR axis in Trp-restricted tumors. SMPD1 inhibitors may, therefore, not only be beneficial to treat EGFR-amplified glioblastomas, as suggested earlier (Bi et al., 2021), but more broadly also Trp-restricted tumors. EGFR-mediated macropinocytosis may also be enhanced by AHR-mediated feedback. This highlights Trp stress as a key event that drives nutrient mobilization by macropinocytosis and autophagy downstream of the EGFR, MTORC1, and the AHR.

Our finding that the depletion of the essential amino acid Trp activates MTORC1 changes our view on the interplay of amino acids with this key tumor driver. MTORC1 is widely recognized as being inactivated by amino acid deprivation. While there is one other study reporting MTORC1 activation in response to glutamine starvation (Chen et al., 2014), this study assigns MTORC1 activation to the overexpression of amino acid transporters. They enhance the influx of amino acids which in turn activate MTORC1. Hence, also this study stays within the common paradigm that amino acid restriction inhibits MTORC1. In contrast, we show that deprivation of an amino acid, namely Trp, directly activates MTORC1. How can this be reconciled with the general notion that amino acids are needed for active MTORC1 signaling? We investigated Trp deprivation in the presence of all other amino acids. Thus, they likely keep MTORC1 at the lysosome, where it is inducible when Trp becomes scarce. This mechanism may have evolved as Trp is the physiologically least abundant amino acid, and a drop in Trp levels is an early indicator of an upcoming starvation for all amino acids. In other words, Trp restriction and activation of the EGFR-MTORC1-AHR axis likely serves as a sentinel mechanism that senses an imminent decline in amino acids. By adapting its translation repertoire, the cell can express proteins that are necessary to cope with nutrient starvation while most amino acids are still sufficiently available. Furthermore, compensation by macropinocytosis and autophagy helps prevent general amino acid shortage. RAS-driven macropinocytosis in cancer enables nutrient uptake and delivers macromolecules for autophagy under conditions when nutrients are scarce (Palm et al., 2015). Macropinocytosis is

broadly recognized to be EGFR dependent and has been known for some time to also be induced by nutrient shortage (Puccini et al., 2022), but the underlying mechanism has remained unclear. We demonstrate that Trp stress directly activates the EGFR-RAS axis, providing a mechanistic link to enhanced macropinocytosis.

The protooncogene RAS is well known to be EGFR-driven. Our finding that Trp restriction activates RAS through the EGFR links RAS to nutrient stress and suggests that RAS not only responds to growth factors but also to metabolic inputs. It is noteworthy that EGFR-RAS-PI3K induction by Trp stress activates MTORC1, specifically towards EIF4EBP1, but not its other *bona fide* substrate RPS6KB1. This is surprising as PI3K is a well-known enhancer of both MTORC1 substrates (Hay and Sonenberg, 2004). Recent evidence shows that the RAG GTPases mediate MTORC1 substrate specificity towards TFEB/TFE (Alesi et al., 2021; Figlia et al., 2022; Gollwitzer et al., 2022; Li et al., 2022; Napolitano et al., 2020), but no differential effect towards RPS6KB1 versus EIF4EBP1 has been described so far. The difference in EIF4EBP1 and RPS6KB1 phosphorylation may be explained by the higher affinity of EIF4EBP1 to the MTORC1 scaffold protein RAPTOR (Bohm et al., 2021; Fumagalli and Pende, 2022), which along with increased EIF4EBP1 levels may enhance recruitment and phosphorylation by MTORC1. Furthermore, stress-responsive MTOR regulators such as Sestrin2 (SESN2) (Ben-Sahra et al., 2013; Budanov and Karin, 2008; Kowalsky et al., 2020; Saxton et al., 2016; Wolfson et al., 2016) may have a role in differential phosphorylation of EIF4EBP1 versus RPS6KB1 and deserve further investigation. It also remains to be determined whether the differential effect extends to other MTORC1 substrates including the autophagy activator ULK1, whose role may be intriguing as Trp restriction enhances autophagy through the MTORC1- EIF4EBP1-AHR axis.

Like MTORC1, translation initiation is also generally considered as being active under nutrient and growth factor sufficiency, whereas it is inhibited by nutrient starvation and stress (Sriram et al., 2018). We report that under Trp stress translation is reduced but remains active. Thus, inhibitory and activating cues concomitantly balance translation under Trp restriction, allowing for expression of a Trp stress protein repertoire. Of note, the proteome in Trp-starved cells still featured Trp containing proteins. As they face a drop in Trp levels, Trp-starved cells mobilize Trp by uptake of extracellular material via macropinocytosis (**Figure 6E and 6F**) and by degrading proteins through autophagy (**Figure 6G - 6P**). Incorporation of phenylalanine (Phe) instead of Trp has recently been suggested to sustain translation in Trp-restricted tumors (Champagne et al., 2021; Pataskar et al., 2022). While there was a low overall frequency of such events in our proteome data, we did not detect an increase in Trp-Phe exchanges upon Trp restriction. Thus,

mobilization of Trp by macropinocytosis and autophagy appears sufficient to sustain translation of the Trp-containing proteome, including the AHR.

Clinical trials with AHR inhibitors are currently ongoing for cancer immunotherapy (Sun, 2021). Our findings demonstrate a novel role for AHR in tumors cells, i.e. enabling them to cope with amino acid limitation. Autophagy promotes tumorigenesis and metastasis in multiple ways including metabolic remodelling and immune evasion (Russell and Guan, 2022). Upon Trp stress, the AHR drives tumor cell autophagy, suggesting that patients with low tumoral Trp / ceramide ratios benefit from autophagy suppression by AHR inhibitors. Even though Trp metabolites enhance AHR activity, we show that reducing Trp in tumors (Badawy, 2018) is not a good strategy to inhibit the AHR as this enhances AHR levels and activity. In tumors with high Trp catabolism, reduced levels of Trp and enhanced levels of Trp catabolites, constituting AHR ligands, likely synergize in boosting AHR activity and its oncogenic outcomes. It has been known for over a decade that Trp depletion synergizes with Trp catabolites (Opitz et al., 2011) and promotes the induction of regulatory T lymphocytes (Treg) (Fallarino et al., 2006) which suppress anti-tumor immunity. New evidence confirms that Trp depletion potentiates the effect of the Trp catabolite kynurenine as an AHR ligand and promotes Treg differentiation (Solvay et al., unpublished, see data availability). This highlights the need to not only consider Trp metabolites but also Trp levels as a biomarker to predict AHR activity in tumors.

Under Trp sufficiency, the AHR has been suggested to suppress autophagy (Guerrina et al., 2021), for instance in response to alcohol, by enhancing PP2A expression and suppressing the autophagy promoting AMP-dependent kinase AMPK (Kim et al., 2022). Likewise, MTORC1 is broadly recognized as a suppressor of autophagy under amino acid rich conditions (Rabanal-Ruiz et al., 2017). Trp restriction switches the AHR into an enhancer of autophagy (**Figure 6K and 6L**). This raises the intriguing perspective that in Trp-starved cells, also MTORC1 turns from a suppressor into an enhancer of autophagy: whereas its canonical outputs towards ULK1 (Hosokawa et al., 2009; Kim et al., 2011) and TFEB/TFE3 (Martina et al., 2012) suppress autophagy, MTORC1's activity towards the EIF4EBP1-AHR axis enhances autophagy under Trp stress. This suggests that under Trp stress, MTORC1-driven AHR activity balances MTORC1's inhibitory effects on autophagy. EGFR, PTEN and RAS transformation indicate autophagy dependence in tumors, and the FDA-approved autophagy inhibitor chloroquine has shown promise in clinical trials (Aquila et al., 2020; Compter et al., 2021; Mulcahy Levy and Thorburn, 2020; Russell and Guan, 2022). Our data broaden this view as a low Trp / ceramide ratio may be indicative of an active EGFR-MTORC1-AHR axis and autophagy addiction, independently of

441 genomic transformation. As a result, Trp restriction along with enhanced ceramides may be a
442 predictor of drug sensitivity to EGFR (Lin et al., 2022), MTORC1 (Pearson and Regad, 2017) and
443 autophagy inhibitors. We advocate testing the tumor Trp / ceramide ratio for patient stratification
444 to these targeted therapies in clinical trials.

445

446 **ACKNOWLEDGEMENTS**

447 We thank the patients from the Heidelberg University Hospital and the tissue bank of the National
448 Center for Tumor Diseases (NCT), the department of Neuropathology Heidelberg, especially
449 Ulrike Vogel. We acknowledge Wilhelm Palm and Rafael Paschoal de Campos for scientific
450 discussions and help with the macropinocytosis assays. We acknowledge the DKFZ Core
451 facilities: Light Microscopy Facility (LMF), especially Damir Krunic (for the help with analysis,
452 microscope introduction), the NGS and OpenLab Core facility (RNAseq). We thank Joram
453 Mooiweer, Julia Sundheimer, Nicholas Zacharewski and Lara Eckhard for their help with harvests
454 and immunoblotting. HS was supported by grants from the Deutsche Forschungsgemeinschaft
455 (DFG) (INST 337/15-1, INST 337/16-1 & INST 152/837-1) TK acknowledges Fellowships from
456 Uehara Memorial Foundation and the International Medical Research Foundation. VIK
457 acknowledges grants from BBSRC (BB/M023389/1, BB/R008167/2). AK was supported by the
458 Austrian Science Fund (FWF) (P 36299) and the Phospholipid Research Center Heidelberg (AKO-
459 2019-070/2-1). AMH acknowledges support by the Tyrolean Science Fund (TWF; grant
460 agreements F.33468/7-2021). KT acknowledges support from Stichting TSC Fonds (calls 2015
461 and 2017), and the German Research Foundation (TH 1358/3-1 and 3-2). MTP (2019) and KT
462 (2017) acknowledge the German TS Foundation. ST, CO and KT acknowledge support from the
463 BMBF e:Med initiative GlioPATH (01ZX1402). CS and KT acknowledge support from the BMBF
464 e:Med initiative MAPTor-NET (031A426A/B). CS, CO, KT, and BvdE acknowledge support from
465 the MESI-STRAT project (grant agreement No 754688) and KT acknowledges support from the
466 PoLiMeR Innovative Training Network (Marie Skłodowska-Curie grant agreement No. 812616)
467 and ARDRE (Marie Skłodowska-Curie grant agreement No. 847681), which have received funding
468 from the European Union's Horizon 2020 research and innovation programme. CH, CO and FS
469 acknowledge support from the German Research Foundation (SFB1389 UNITE-Glioblastoma;
470 project No. 404521405). SM acknowledges support from the German Academic Exchange
471 Service. KT acknowledges support from the European Partnership for the Assessment of Risks
472 from Chemicals PARC which has received funding from the European Union's Horizon Europe
473 research and innovation programme under Grant Agreement No. 101057014. KT was recipient of

a Rosalind-Franklin-Fellowship of the University of Groningen and of the Research Award of the German Tuberous Sclerosis Foundation 2017. MS was a Research Fellow of the F.R.S.-FNRS (Belgium; Grant No 1.A.385.16). BVdE acknowledges support from the EOS consortium DECODE (Belgium, Grant No 30837538). FL-P acknowledges support from the ERC-STG DualRP project (Grant agreement ID: 759579).

## AUTHOR CONTRIBUTIONS

PP, LH, PRN and MTP designed and performed experiments, analysed data, and wrote materials & methods and figure captions. MS conducted and analysed experimental data. AS designed, performed and wrote bioinformatics methods and analyses for cancer transcriptome and RPPA data. AH designed experiments and contributed to scientific discussions. SS and LR designed and performed experiments and analysed data. TB performed MALDI-MS Imaging. ASE developed, performed and analysed intracellular Trp measurements and analysed proteome data. BB, IK, LFSP, MR, DS, VP, TK, MH, JRP, ILK, TB performed and supported experiments and analyses. ST performed promotor analysis. AvP and YZ supported proteome sample preparation and data analysis. FL-P and AK performed ribosome profiling. SK measured the proteome. LW established and AG and LW performed MS lipid analyses and analysed lipid MS data. TK and VK perfomed autophagy gene analysis and supported autophagy data analysis. SM performed analysis of MALDI-MS imaging. PS, FS performed tissue collection and pathological assessment. HS supervised proteome measurement. AK supervised lipid measurements. CH supervised MALDI-MS Imaging. MK designed and supervised proteome and intracellular Trp measurement and analysis. CS designed and supervised EGFR and RAS experiments and LAMP stainings. BVdE analysed data and contributed to scientific discussions. CO and KT conceived and supervised the study, designed and analysed experiments, and wrote the manuscript. All the authors read, revised, and approved the manuscript.

## DECLARATION OF INTERESTS

AS, ST and CO are founders and AS and CO are managing directors of cAHRmeleon Bioscience GmbH. VIK is a Scientific Advisor for Longaevus Technologies. Authors of this manuscript have patents on AHR inhibitors in cancer (WO2013034685, CO); A method to multiplex tryptophan and its metabolites (WO2017072368, CO); A transcriptional signature to determine AHR activity (WO2020201825, AS, ST, CO); Interleukin-4-induced gene 1 (IL4I1) as a biomarker

506 (WO2020208190, AS, ST, LFSP, MPT, CO) Interleukin-4-induced gene 1 (il4i1) and its
507 metabolites as biomarkers for cancer (WO2021116357, AS, ST, LFSP, CO).

**Figure 1: Tryptophan (Trp) restriction enhances EIF4EBP1 (4E-BP1) phosphorylation through MTORC1 and PIK3CA (PI3K).**

(A) MALDI mass spectrometry imaging (MALDI MSI) of Trp distribution in human glioblastoma (GB) sections (n = 3). Color scale: purple, low Trp; yellow, high Trp; scale bar: 1 mm.

(B) Translation under Trp sufficiency or starvation. Puromycin (5 µg/mL, 5 min) incorporation in LN-18 glioblastoma cells, unstimulated or stimulated with epidermal growth factor (EGF, 10 ng/mL, stimulation period as indicated), and treated with the translation elongation inhibitor cycloheximide (CHX) (2 µg/mL, 6.5 h) (n = 4).

(C) Quantification of puromycin incorporation in (B). Three replicates were normalized to GAPDH, one replicate to VCL (vinculin).

(D) Signaling towards translation initiation under Trp stress. Trp concentration row in LN-18 cells (n = 3), except EIF4EBP1-pT37/46 (4E-BP1-pT37/46) (n = 4).

(E) Quantification of EIF2A-pS51 in (D).

(F) Quantification of EIF4EBP1 (4E-BP1) in (D).

(G) Quantification of RPS6KB1-pT389 (S6K-pT389) in (D).

(H) Quantification of EIF4EBP1-pT37/46 (4E-BP1-pT37/46) in (D).

(I) Quantification of EIF4E-pS209 in (D).

(J) Trp-restricted LN-229 glioblastoma cells also exhibit enhanced phosphorylation of both EIF4EBP1-T37/46 (4E-BP1-pT37/46) and EIF4E-S209. Cells were stimulated with EGF (10 ng/mL) for the indicated time periods (n = 4).

(K) Quantification of EIF4EBP1-pT37/46 (4E-BP1-pT37/46) in (J).

(L) Quantification of EIF4E-pS209 in (J).

(M) Quantification of RPS6KB1-pT389 (S6K-pT389) in (J).

(N) The MTOR inhibitor AZD8055 blocks EIF4EBP1-pT37/46 (4E-BP1-pT37/46) under Trp stress. LN-18 cells stimulated with EGF (10 ng/mL, 15 min) and treated with AZD8055 (100 nM, 1 h) (n = 3).

(O) Quantification of EIF4EBP1-pT37/46 (4E-BP1-pT37/46) in (N).

(P) The MTOR inhibitor AZD8055 blocks EIF4EBP1-pT37/46 (4E-BP1-pT37/46) and EIF4EBP1-pT70 under Trp stress. LN-18 cells treated with AZD8055 (100 nM, 24 h) (n = 4).

(Q) Quantification of EIF4EBP1-pT37/46 (4E-BP1-pT37/46) in (P).

(R) Quantification of EIF4EBP1-pT70 (4E-BP1-pT70) in (P).

(S) PIK3CA (PI3K) inhibition with GDC0941 (1 µM, 1 h) blocks Trp stress induced EIF4EBP1-pT37/46 (4E-BP1-pT37/46). LN-18 cells were stimulated with EGF (10 ng/mL, 15 min) as indicated (n = 4).

(T) Quantification of EIF4EBP1-pT37/46 (4E-BP1-pT37/46) in (S). Two replicates were normalized to TUBA1B (tubulin) and two replicates were normalized to GAPDH.

Cells were cultured in presence of Trp (+Trp, grey, 78 µM), absence of Trp (-Trp, blue, 0 µM) or in presence of the indicated Trp concentrations for 24 h. One-way ANOVA followed by a Šídák's multiple comparisons test was applied (C, E – I, O, Q, R, T). Time courses with more than two conditions were compared using a two-way ANOVA (Figures K – M). Data are presented as mean ± SEM. *p < 0.05, **p < 0.01, ***p < 0.001. n.s., not significant.

**Figure 2: Upon Trp stress, p38 signals to EIF4E, and RAS signals to both EIF4EBP1 (4E-BP1) and EIF4E.**

(A) MAP2K (MEK) inhibition with AZD6244 (1 µM, 1 h) does not reduce EIF4E-pS209 induction by Trp stress. LN-18 cells were stimulated with EGF (10 ng/mL, 15 min) as indicated (n = 4).
(B) Quantification of MAPK1/3-pT202/204 (ERK1/2) in (A).
(C) Quantification of EIF4E-pS209 in (A).

(D) p38α/β inhibition by LY2228820 (1 µM, 1 h) reduces EIF4E-pS209 induction by Trp stress. LN-18 cells were stimulated with EGF (10 ng/mL, 15 min) as indicated (n = 3).
(E) Quantification of MAPKAPK2-pT334 (MK2-pT334) in (D).
(F) Quantification of EIF4E-pS209 in (D).

(G) Pan-RAS knockdown (siKRAS/HRAS/NRAS) reduces EIF4EBP1-pT37/46 and EIF4E-pS209 induction by Trp stress. LN-18 cells were stimulated with EGF (10 ng/mL, 15 min) as indicated (n = 6).
(H) Quantification of KRAS/HRAS/NRAS in (G).
(I) Quantification of EIF4EBP1-pT37/46 (4E-BP1-pT37/46) in (G).
(J) Quantification of EIF4E-pS209 in (G).

(K) Trp stress enhances RAS-GTP binding to RAF1-GST. RAS activity was measured using GST-coupled RAF-RAS–binding domain pull down experiments. RAF1-GST pulldown from LN-18 cells treated with EGF (10 ng/mL, 30 min) (n = 4).
(L) Quantification of RAS-GTP in (K).

Cells were cultured in presence of Trp (+Trp, grey, 78 µM) or absence of Trp (-Trp, blue, 0 µM) for 24 h. One-way ANOVA followed by a Šídák's multiple comparisons test was applied (B, C, E, F, H, I, J). For (L) a two-tailed paired Student’s t test was performed. Data are presented as mean ± SEM. *p < 0.05, **p < 0.01, ***p < 0.001. n.s., not significant.

**Figure 3: Trp restriction activates EGF receptor signaling to EIF4EBP1 (4E-BP1) and EIF4E.**

(A) Trp deprivation enhances autophosphorylation of the EGFR at Y1068. LN-18 cells were stimulated with EGF (10 ng/mL, 15 min) (n = 3). Detections of the same samples as in Figure 1S (lanes 1 to 4).
(B) Quantification of EGFR-pY1068 in (A). Two replicates normalized to TUBA1B (tubulin). One replicate normalized to GAPDH.

(C) Low Trp levels enhance autophosphorylation of the EGFR at Y1068. Trp concentration row in LN-18 cells (n = 3). Detections of the same samples as in Figure 1D.
(D) Quantification of EGFR-pY1068 in (C).

(E) Trp starvation enhances EGFR internalization to perinuclear endosomes. Immunofluorescence (IF) of EGFR localization. LN-18 cells were stimulated with EGF (10 ng/mL, 15 min). Scale bar: 10 µm (n = 4).
(F) Quantification of EGFR (foci per 100 cells) in (E).

(G) The pan-ERBB receptor inhibitor Afatinib (10 µM, 1 h) inhibits Trp restriction induced EIF4EBP1-pT37/46 and EIF4E-pS209. LN-18 cells were stimulated with EGF (10 ng/mL, 30 min) (n = 5).
(H) Quantification of EIF4EBP1-pT37/46 (4E-BP1-pT37/46) in (G).
(I) Quantification of EIF4E-pS209 in (G).

(J) *Epidermal growth factor* (*EGF)* mRNA relative to *18S rRNA* measured by qRT-PCR upon Trp restriction in LN-18 cells (n = 3).
(K) *Epiregulin (EREG)* mRNA relative to *18S rRNA* measured by qRT-PCR upon Trp restriction in LN-18 cells (n = 4).

(L) Low Trp levels enhance non-glycosylated and glycosylated pro-epiregulin (pro-EREG). Trp concentration row in LN-18 cells (n = 3). Detections of the same samples as in Figure 1D.
(M) Quantification of pro-EREG in (L).
(N) Quantification of glycosylated pro-EREG in (L).

(O) Pan-ERBB receptor inhibitor Afatinib (10 µM, 1 h) and EGFR-specific inhibitor Erlotinib (10 µM, 1 h) inhibit Trp restriction induced EIF4EBP1-pT37/46 (4E-BP1-pT37/46) and EIF4E-pS209. LN-18 cells were stimulated with EGF (10 ng/mL, 30 min) (n = 3).

(P) Quantification of EGFR-pY1068 in (O).

(Q) Quantification of EIF4EBP1-pT37/46 (4E-BP1-pT37/46) in (O).

(R) Quantification of EIF4E-pS209 in (O).

Cells were cultured in presence of Trp (+Trp, grey, 78 µM), absence of Trp (-Trp, blue, 0 µM) or in the presence of the indicated Trp concentrations for 24 h. One-way ANOVA followed by a Šídák's multiple comparisons test was applied (B, D, F, H, I, M, N, P – R). For (J) and (K) a two-tailed paired Student's t test was performed. Data are presented as mean ± SEM. *p < 0.05, **p < 0.01, ***p < 0.001, n.s., not significant.

**Figure 4: The MTORC1-EIF4EBP1 (4E-BP1) axis enhances translation of the AHR under Trp stress.**

(A) The EIF4EBP1 (4E-BP1) agonist 4EGI-1 (10 µM, 24 h) inhibits translation upon Trp stress. CHX, translation elongation inhibitor cycloheximide (2 µg/mL, 24 h). Puromycin (5 µg/mL, 5 min) incorporation in LN-18 cells (n = 3).
(B) Quantification of puromycin incorporation in (A).

(C) The MTOR-inhibitor AZD8055 (100 nM, 4 h) inhibits translation upon Trp stress. CHX, cycloheximide (2 µg/mL, 4 h). Puromycin (5 µg/mL, 5 min) incorporation in LN-18 cells. (n = 3).
(D) Quantification of puromycin incorporation in (C).
(E) Quantification of EIF4EBP1-pT37/46 (4E-BP1-pT37/46) in (C).

(F) The Trp stress proteome reveals increase of the aryl hydrocarbon receptor (AHR). Trp sufficiency (+Trp) was compared to Trp stress (-Trp). Volcano plot of protein abundances in LN-18 cells (n = 3).
(G) Gene Ontology (GO) terms related to macropinocytosis and lysosomes are enriched in the Trp stress proteome. GO enrichment analysis of proteins upregulated under Trp stress (-Trp) in (F). Proteins were considered to be upregulated with FC ≥ 1.5 and an adjusted p-value < 0.05. The length of the bar represents the $\log_{10}$ Benjamini-Hochberg corrected p-value. Indicated for each term is the number of associated proteins in the Trp stress proteome; in brackets: total number of associated proteins per term. Proteins that belong to the GO terms in (G) are marked in the corresponding colors in the volcano plot (F).

(H) AHR levels are increased by Trp stress in a concentration-dependent manner. Trp concentration row in LN-229 cells (n = 5).
(I) Quantification of AHR in (H).

(J) Ribosomes exhibit increased association with AHR transcripts upon Trp stress. Ribosome profile: Ribosome protected fragment (RPF) read density is shown on the AHR transcript (genomic location, chr7:17,338,276-17,385,775; hg19) in LN-229 cells in the presence and absence of Trp. Reads per transcript normalized to total number of reads are shown on the y-axis (n = 1). Bottom panel, short rectangles represent untranslated regions, tall rectangle indicates coding sequence.

(K) The pan-ERBB inhibitor Afatinib (10 µM, 24 h) suppresses AHR induction by Trp stress in LN-229 cells (n = 4-5).
(L) Quantification of AHR in (K).
(M) Quantification of EIF4EBP1-pT37/46 (4E-BP1-pT37/46) in (K).
(N) Quantification of EIF4E-pS209 in (K).

(O) The MTOR inhibitor AZD8055 (100 nM, 24 h) suppresses AHR induction by Trp stress in LN-229 cells (n = 5).
(P) Quantification of AHR in (O).
(Q) Quantification of EIF4EBP1-pT37/46 (4E-BP1-pT37/46) in (O).

(R) The EIF4EBP1 (4E-BP1) agonist 4EGI-1 (10 µM, 24 h) suppresses AHR induction by Trp stress in LN-229 cells (n = 3).
(S) Quantification of AHR in (R).

(T) Cycloheximide (CHX) (5 µg/mL, 24 h) suppresses AHR induction by Trp stress in LN-229 cells (n = 4).
(U) Quantification of AHR in (T).

Cells were cultured in presence of Trp (+Trp, grey, 78 µM), absence of Trp (-Trp, blue, 0 µM) or in the presence of the indicated Trp concentrations for 24 h. One-way ANOVA followed by a Šídák's multiple comparisons test was applied (B, D, E, I, L – N, P, Q, S, U). Data are presented as mean ± SEM. *$p < 0.05$, **$p < 0.01$, ***$p < 0.001$. n.s., not significant.

**Figure 5: The p38-EIF4E-ATF4 axis enhances AHR levels under Trp stress.**

(A) The p38α/β inhibitor LY2228820 (1 µM, 24 h) suppresses AHR induction by Trp stress in LN-229 cells (n = 4).

(B) Quantification of AHR in (A).

(C) Quantification of EIF4E-pS209 in (A).

(D) The MKNK1 (MNK1) inhibitor CGP-57380 (20 µM, 24 h) suppresses EIF4E-pS209, but does not affect overall translation upon Trp stress. CHX, cycloheximide (2 µg/mL, 24 h). Puromycin (5 µg/mL, 5 min) incorporation in LN-18 cells (n = 3).

(E) Quantification of puromycin incorporation in (D).

(F) Quantification of EIF4E-pS209 in (D).

(G) ATF4 translation is enhanced upon Trp stress. Ribosome profiling: Ribosome protected fragment (RPF) read density is shown on the ATF4 transcript (genomic location, chr22:39,916,569-39,918,691; hg19) in LN-229 cells in the presence and absence of Trp. Reads per transcript normalized to total number of reads are shown on the y-axis (n = 1). Bottom panel, short rectangles represent untranslated regions, tall rectangle indicates coding sequence. Analysis of the same dataset as in Figure 4J.

(H) The p38α/β inhibitor LY2228820 (1 µM, 24 h) suppresses ATF4 induction by Trp stress in LN-229 cells (n = 4). Detections of the same samples as in (A).

(I) Quantification of ATF4 in (H).

(J) Graphical representation of an ATF4 (TRANSFAC, V_ATF4_Q6_M01864) binding site upstream of the AHR transcription start site. The chromatin landscape information was adapted from the UCSC browser, showing histone H3 acetylation of the N-terminal position of lysine 27 (H3K27Ac), a DNase hypersensitivity cluster (ENCODE v3) and chromatin state segmentation based on ChromHMM.

(K) ATF4 knockdown suppresses AHR induction by Trp stress in LN-229 cells (n = 3).

(L) Quantification of ATF4 in (K).

(M) Quantification of AHR in (K).

(N) The MTOR inhibitor AZD8055 (100 nM, 24 h) partially inhibits AHR induction by Trp stress in LN-229 cells (n = 4). Detections of the same samples as in Figure 4O.
(O) Quantification of ATF4 in (N).

(P) The pan-ERBB inhibitor Afatinib (10 µM, 24 h) inhibits AHR induction by Trp stress in LN-229 cells (n = 4). Detections of the same samples as in Figure 4K.
(Q) Quantification of ATF4 in (P).

(R) EIF2AK4 (GCN2) knockdown does not affect AHR induction by Trp stress in LN-229 cells (n = 3).
(S) Quantification of EIF2AK4 (GCN2) in (R).
(T) Quantification of AHR in (R).
(U) Quantification of ATF4 in (R).

Cells were cultured in presence of Trp (+Trp, grey, 78 µM) or absence of Trp (-Trp, blue, 0 µM) for 24 h. One-way ANOVA followed by a Šídák's multiple comparisons test was applied (B, C, E, F, I, L, M, O, Q, S – U). Data are presented as mean ± SEM. *$p < 0.05$, **$p < 0.01$, ***$p < 0.001$. n.s., not significant.

**Figure 6: Trp stress induced AHR enhances autophagy to replenish intracellular Trp.**

(A-B) AHR is active upon Trp stress in LN-18 (A) and LN-229 (B) cells as determined by the induction of the AHR target gene *CYP1B1.* mRNA expression was measured relative to *18S rRNA* by qRT-PCR (n = 4).

(C-D) RNAseq analysis reveals an enhanced transcriptional AHR activity signature in LN-18 (C) and LN-229 (D) cells upon Trp stress. Barcode plots showing the status of AHR activity in RNAseq data of LN-18 (C) and LN-229 (D) cells starved for 24 h with Trp (n = 4). The x-axis represents the values of moderated t-statistic values for all genes in the comparison. The blue and pink colored segments represent the lower and upper quartiles of all the genes. The vertical barcode lines represent the distribution of the genes. The worm line above the barcode shows the relative density of the AHR-signature genes, which represents the direction of regulation.

(E) Trp stress increases the area of intracellular macropinosomes. Uptake assay of fluorescently labelled 70 kDa - dextran (dextran) in LN-18 cells stained with DAPI, stimulated with EGF (10 ng/mL, 30 min). Scale bar: 10 µm (n = 4).
(F) Quantification of area of macropinosomes in (E).

(G) Trp stress increases the lysosomal compartment size. Immunofluorescence staining of LAMP2 in LN-18 cells, stimulated with EGF (10 ng/mL, 15 min). Scale bar: 10 µm (n = 4).
(H) Quantification of LAMP2 area (compartment size) per cell in (G).

(I) Trp stress increases the lysosomal activity. Live cell imaging of LysoTracker Red DND-99 (lysotracker, 30 min) and DAPI in LN-18 cells. Scale bar: 10 µm (n = 5).
(J) Quantification of intensity of lysotracker foci in (I).

(K) Trp stress enhances autophagic flux (Bafilomycin $A_1$ induced MAP1LC3B lipidation) in an AHR-dependent manner. Bafilomycin $A_1$ (100 nM, 2 h) and AHR inhibitor SR1 (1 µM, 24 h) treated LN-18 cells (n = 5).
(L) Quantification of MAP1LC3B-II (LC3-II) in (K).

(M) An autophagy mRNA signature is enriched upon Trp stress. Barcode plot showing enrichment of autophagy regulators in RNAseq data of LN-18 cells starved of Trp for 24 h (n = 4). Analysis of the same dataset as in (C).

(N) Comparison of genes differentially regulated by Trp sufficiency (+Trp) versus Trp stress (-Trp) in RNAseq data of LN-18 cells. Autophagy-related genes are colored in cyan. AHR, MAP1LC3B (LC3) and ATG13 are shown in red (n = 4). Analysis of the same dataset as in (C).

(O) Interaction network analysis of reported physical interactions between autophagy-related components identified in (N). Clusters generated by k-means clustering were arbitrarily classified based on their functions.

(P) Cells under Trp stress exhibit a further decrease in intracellular Trp when lysosomal function is inhibited. Intracellular Trp concentration in LN-18 cells with and without Bafilomycin $A_1$ (100 nM, 2 h) (n = 4).

Cells were cultured in the presence of Trp (+Trp, grey, 78 µM) or absence of Trp (-Trp, blue, 0 µM) for 24 h. One-way ANOVA followed by a Šídák's multiple comparisons test was applied (L, P). For (A), (B), (F), (H) and (J) a two-tailed paired Student’s t test was performed. For bioinformatics analysis, statistic is described in the Method Details section (C, D, M, N, O). Data are presented as mean ± SEM. *p < 0.05, **p < 0.01, ***p < 0.001, n.s., not significant.

**Figure 7: Glioblastoma exhibit an induced MTOR-EIF4EBP1-AHR axis, enhanced autophagy regulators and mutually exclusive areas of Trp and ceramides.**

(A, B) Distribution of the (A) AHR activity score and (B) the normalized expression values of AHR in the seven glioblastoma patient subgroups. The black dotted line represents the mean AHR activity score or normalized AHR expression values across all patient samples. The p-values were determined based on comparing the average score or expression to the corresponding mean of all patient sample groups.

(C) The group with high AHR activity and AHR levels (group 2, blue) exhibits higher EIF4EBP1-pT37/46 (4E-BP1-pT37/46) levels compared to group 1 (grey) with high AHR activity but low AHR levels. Shown is the distribution of the RPPA values of EIF4EBP1-pT37/46 (4E-BP1-pT37/46) in groups 1 and 2.

(D) The two patient groups with high AHR activity show similar levels of RPS6KB1 (S6K) phosphorylation. Shown is the distribution of the RPPA values of P70S6K1-pT389 (S6K-pT389) in groups 1 and 2.

(E) Group 2 with high AHR activity and AHR levels shows enhanced expression of autophagy regulators. Shown is the distribution of the single sample enrichment scores of gene sets of autophagy regulators in groups 1 and 2.

(F) Trp stress enhances the cellular proportion of ceramides in an AHR-dependent manner. Ceramide ratio of total sphingolipids in LN-18 cells, cultured in presence (+Trp, grey, 78 µM) or absence (-Trp, blue, 0 µM) of Trp and the AHR inhibitor SR1 (1 µM, 24 h) for 24 h (n = 7).

(G) In human glioblastoma, regions of high Trp and high ceramides are mutually exclusive. MALDI MSI of Trp and ceramide hotspots and their intersections in human glioblastoma samples (n = 4). Scale bar: 1 mm.

A two-tailed unpaired Student's t test was performed in (F). For bioinformatic analysis, statistic is described in the Method Details section (A-E). Data are presented as mean ± SEM. *p < 0.05, **p < 0.01, ***p < 0.001. n.s., not significant.

# STAR METHODS

## CONTACT FOR REAGENT AND RESOURCE SHARING

Further information and requests for resources and reagents should be directed to and will be fulfilled by the lead contact, Kathrin Thedieck (kathrin.Thedieck@uibk.ac.at).

## MATERIALS AVAILABILITY

All unique materials and reagents generated as part of this study are available from the lead contact with a completed Material Transfer Agreement.

## DATA AND CODE AVAILABILITY

A BioRxiv citation for the unpublished manuscript of Solvay et al. will be added.

## EXPERIMENTAL MODEL AND SUBJECT DETAILS

### Cell culture and treatments

Glioblastoma cell lines LN-18 and LN-229 were obtained from ATCC and regularly authenticated by multiplex human cell line authentication assay (MCA) at Multiplexion. The cells were cultured at 37 ºC and 5% $CO_2$ and regularly tested for mycoplasma contamination. Cells were cultured in DMEM (Biotech, P04-03600) with 4.5 g/L glucose, supplemented with 2 mM L-glutamine (Gibco, 25030-024) or in phenol red-free DMEM (Gibco, 31053-028) with 10% FBS (Gibco, 10270106) and 2 mM L-glutamine (Gibco, 25030-024), 1 mM sodium pyruvate (Gibco, 11360039), 100 U/mL penicillin and 100 µg/mL streptomycin (Gibco, 15140122).

For Trp starvation experiments, customized Trp-free DMEM (Gibco, ME15175L1) containing 4.5 g/L glucose was supplemented with either 10% dialyzed FBS (Life Technologies, 26400044), 2 mM L-glutamine (Gibco, 25030-024), 1 mM sodium pyruvate (Gibco, 11360039) and 100 U/mL penicillin and 100 µg/mL streptomycin (Gibco, 15140122) or only supplemented with 2 mM L-glutamine (Gibco, 25030-024). Trp was dissolved in cell culture grade water (Corning, 25-055-CV) and added fresh at a final concentration of 78 µM (or titrated as indicated) or complete DMEM (Gibco, 31053-028) was used as Trp-containing control medium.

For MTOR pathway analysis, one day before starvation, 1 x $10^6$ LN-18 or LN-229 cells per plate were seeded in 6 cm plates containing complete DMEM (Biotech, P04-03600). The next day, cells were washed twice with PBS (Biotech, Cat# P04-36500) and Trp-containing (Gibco, 31053-028) or Trp-free DMEM (Gibco, ME15175L1) medium (supplemented with 2 mM L-glutamine (Gibco, 25030-024)) was added for the 24 h.

EGF (Peprotech, AF-100-15) was diluted in PBS (SERVA, 47302.03) with 0.1% BSA (Carl Roth, 8076.5) and added directly into the media at a final concentration of 10 µg/mL for the indicated time points. Cycloheximide (Sigma-Aldrich, C4859) was diluted in water and directly added to the media at a final concentration of 2 µg/mL for the indicated time points. Inhibitors were diluted in DMSO (Sigma-Aldrich, D2650) and cells were treated with 10 µM 4EGI-1 (Tocris, 4800), 10 µM Afatinib (Selleckchem, S1011), 1 µM AZD6244 (MedChem Express, HY-50706), 100 nM AZD8055 (MedChem Express, HY-10422), 100 nM Bafilomycin A1 (MedChem Express, HY-100558), 20 µM CGP-57380 (Axon, 1611), 10 µM Erlotinib (Selleckchem, S7786), 1 µM GDC0941 (Axon, 1377), 1 µM LY2228820 (Axon Medchem, 1895) and 1 µM SR1 (Merck Millipore, 182706) for the indicated time points.

For analysis of AHR expression and activation, 4 x $10^5$ LN-229 cells per well were seeded in six-well plates in complete DMEM (Gibco, 31053-028). The next day, cells were washed with PBS (Gibco, 14190169) and Trp-supplemented (78 µM) or Trp-free DMEM (Gibco, ME15175L1) (supplemented with 10% dialyzed FBS (Life Technologies, 26400044), 2 mM L-glutamine (Gibco, 25030-024), 1 mM sodium pyruvate (Gibco, 11360039) and 100 U/mL penicillin and 100 µg/mL streptomycin (Gibco, 15140122)) with or without inhibitors or DMSO was added for 24 h. Inhibitors were diluted in DMSO (Carl Roth, 4720) and cells were treated with 10 µM Afatinib (Selleckchem, S1011), 100 nM AZD8055 (MedChem Express, HY-10422) and 1 µM LY2228820 (Selleckchem, S1494). Cycloheximide solution (Sigma-Aldrich, C4859) was diluted to a final concentration of 5 µg/mL and added for 24 h.

**Generation of transgenic cell lines**

Transient siRNA-mediated knockdown

siRNA knockdown of KRAS/HRAS/NRAS was induced using 10 nM of each KRAS, HRAS and NRAS (total siRNA 30 nM) ON-TARGETplus human SMARTpool siRNA (Dharmacon, L-005069-00-0005, L-004142-00-0005, L-003919-00-0005) for 8 h followed by a medium change. Transfections were preformed using Lipofectamine 3000 (Invitrogen, L3000008) according to the manufacturer's protocol 48 h before cells were cultured in Trp-containing or Trp-free medium for 24 h. As a control, non-targeting scramble siRNA (siControl, Dharmacon, D-001810-10-05) was used at the same concentration.

For siRNA-mediated knockdown of ATF4 and GCN2 ON-TARGETplus human SMARTpool siRNA reagents (Dharmacon, L-010351-00-0005 and L-005314-00-0005) were used at a final concentration of 40 nM for 8 h followed by a medium change. Transfection was performed with Lipofectamine RNAiMAX (Thermo Fisher Scientific, 13778100) according to the manufacturer´s

protocol 24 h before cells were cultured in Trp-containing or Trp starvation medium for 24 h. ON-TARGETplus non-targeting pool siRNA (Dharmacon, D-001810-10-05) was used as a control at the same concentration. Knockdown efficiency was confirmed by gene and protein expression analysis using qRT-PCR and immunoblot.

## METHOD DETAILS

### Human glioblastoma samples

Tumor specimens of patients diagnosed with glioblastoma (WHO grade IV, IDH wildtype) were obtained from the Institute of Neuropathology, Heidelberg University Hospital, according to the regulations of the Tissue Bank of the National Center for Tumor Diseases (NCT), Heidelberg University Hospital, under the ethics board approval S-318/2022. Glioblastoma samples were cut into 10 µm thick sections with a CM1950 cryostat (Leica Biosystems) and mounted onto ITO coated glass slides (Bruker Daltonics, 8237001) for MALDI MS Imaging. Slides were stored in slide boxes (neoLab, 2-3080), covered with foil, vacuumed (CASO) and stored at -80°C until further processing. Consecutive tissue sections were stained with hematoxylin and eosin (HE) and annotation of tumor tissue regions was performed by a clinically experienced neuropathologist.

### MALDI mass spectrometry imaging (MSI)

<u>MALDI MSI sample preparation</u>

Immediately before matrix coating, the frozen slides were equilibrated at RT and dried for 10 min in a desiccator (SP Bel-Art). 100 µL of a 5 mg/mL deuterated tryptophan (D5-Trp) solution (Cayman Chemicals, 34829) in ACN/H2O (50:50, v/v) (Honeywell, 34967) was added to 25 mg/mL 2,5-dihydroxybenzoic acid (Alfa Aesar, A11459) in ACN/H2O/TFA (49.4:49.4:0.2, v/v/v) (Merck KGaA, 1.08262.0025) solution and sprayed onto tissue sections with the following parameters: nozzle temperature 75°C, 12 layers, flow rate 0.11 mL/min, velocity 1200, track spacing 2 mm, pattern CC, pressure 10 psi, dry time 0s, nozzle height 40 mm.

<u>Magnetic resonance MALDI MS imaging data acquisition</u>

Data acquisition was performed on a Fourier-transform ion cyclotron resonance (FT-ICR) magnetic resonance mass spectrometer (MRMS; solariX XR 7T, Bruker Daltonics) in two steps (**Table 1**). First, method 1 optimized for detection of Trp was used at 100 µm step-size. Thereafter, method 2 optimized for detection of ceramides was used on the same tissue section with an XY-

offset of 50 µm at step-size 100 µm. Peak filtering was set to SNR > 3 and an absolute intensity threshold of $10^5$ a.u.

**Table 1. MRMS MALDI acquisition methods.**

| | Method 1 optimized for Trp | Method 2 optimized for Ceramides |
|---|---|---|
| **Online calibration** | D5-Trp 210.128538 | PC (34:1) 760.585082 |
| **Size** | 4M | 2M |
| **Mass range** | m/z 75-800 | m/z 300-800 |
| **Transient length** | 1.47 sec | 2.93 sec |
| **Resolving power at m/z 400** | 200,000 | 390,000 |
| **Laser shots** | 300 | 300 |
| **Frequency** | 2000 Hz | 2000 Hz |
| **Laser focus** | small | small |
| **Q1 Mass** | 200 | 500 |
| **Funnel RF amplitude** | 80 V | 120 V |
| **Time of flight** | 0.5 ms | 0.5 ms |
| **Q1 isolation** | 200 ± 100 | off |

Centroided data was imported into SCiLS Lab 2023a Pro software (Bruker Daltonics), then exported as .imzml file and uploaded to the Metaspace platform (https://metaspace2020.eu/) for annotation of metabolites. Raw spectra were evaluated in DataAnalysis software (Bruker Daltonics), and the smart formula function was used to generate sum formulas that supported the annotations in METASPACE.

Data Processing

Tissue areas were selected using an in-house-built IT tool and saved as regions of interest (ROI) in the raw data file. Data processing was done in R (version 4.2.1). First, centroided data was loaded, data for every ROIs per tissue sample was extracted using an in-house-built R-tool. The data was loaded as a sparse matrix representation using Matrix package, for faster matrix processing. Next, full width at half maximum (FWHM) was calculated as a function of *m/z* per sample, using the *moleculaR* package (Sammour et al., 2021). This was followed by peak binning using the MALDIquant package (Gibb and Strimmer, 2012), and intensity normalization using *moleculaR* package [Root Means Square (RMS) for ceramides-focused datasets and internal standard (IS; D5-tryptophan *m/z* 210.12854) for tryptophan-focused datasets]. Finally, peak filtering was performed with a minimum frequency set to 0.01.

Calculation of molecular probability maps (MPMs) and collective projection probability maps (CPPMs)

Ceramide adduct masses ($[M+H]^+$, $[M+Na]^+$, and $[M+K^+]$) were extracted from the LipidMaps database (www.lipidmaps.org). The data representation was first converted from raw ion intensities into spatial point patterns representations, and then MPMs were calculated per molecule (one ceramide or Trp) of interest (MOI). Subsequently, MPMs for each of the ceramides were standardized and then converted into CPPM representation, as described in Abu Sammour *et al.*, 2021 (Sammour et al., 2021). Hotspot areas and contours that indicate significantly increased MOI presence were generated for each tissue sample using the *Spatstat R* package.

Calculation of Dice Similarity Coefficient (DSC) values

To calculate overlap between Trp's MPM hotspot contours with each of the ceramides' CPPM hotspot contours, Dice Similarity Coefficient (DSC) was calculated as described in Abu Sammour *et al.*, 2021 (Sammour et al., 2021).

**RNA isolation, cDNA synthesis and qRT-PCR**

For RNA isolation, cells were harvested using RTL buffer containing 10 µL/mL beta-mercaptoethanol (Sigma-Aldrich, M3148) and isolated as recommended in the manufacturer´s protocol of the RNeasy Mini Kit (Qiagen, 74106). DNAse digest step was performed as recommended in the protocol using the RNase free DNAse kit (Qiagen, 79254). RNA concentration and quality were determined by Nanodrop (Thermo Fisher Scientific). Subsequently, cDNA was synthetized using 1 µg RNA and the High Capacity cDNA reverse transcriptase kit (Applied Biosystems, 4368813). Quantitative real-time PCR (qRT-PCR) was performed in a 96-well format using the StepOne Plus Real-Time PCR system (Applied Biosystems) and SYBR Select Master Mix (Thermo Fisher Scientific, 4364346). Expression data was processed using StepOne Software v2.3 (Thermo Fisher Scientific) and analyzed with the $2^{-\Delta\Delta Ct}$ method using *18S rRNA* as reference gene. All primers used in this study are listed in Table S1.

**RNA sequencing**

For RNA sequencing, 4 x $10^5$ LN-229 or LN-18 cells per well were seeded in six-well pates. On the next day, cells were washed with PBS (Gibco, 14190169) and cultivated for 24 h in Trp-supplemented (78 µM) or Trp-free DMEM supplemented with 10% dialyzed FBS (Life

Technologies, 26400044), 2 mM L-glutamine (Gibco, 25030-024), 1 mM sodium pyruvate (Gibco, 11360039) and 100 U/mL penicillin and 100 µg/mL streptomycin (Gibco, 15140122) prior to harvest. RNA isolation was performed as described above. Illumina sequencing libraries were prepared using the TruSeq Stranded mRNA Library Prep Kit (Illumina, 20020595) according to the manufacturer's protocol. Briefly, poly(A)+ RNA was purified from a maximum of 500 ng of total RNA using oligo(dT) beads, fragmented to a median insert length of 155 bp and converted to cDNA. The ds cDNA fragments were then end-repaired, adenylated on the 3′ end, adapter ligated and amplified with 15 cycles of PCR. The libraries were quantified using Qubit ds DNA HS Assay kit (Life Technologies-Invitrogen, Q33231) and validated on an Agilent 4200 TapeStation System (Agilent technologies, 5067-5582, 5067-5583). Based on Qubit quantification and sizing analysis multiplexed sequencing libraries were normalized, pooled and sequenced using the NovaSeq 6000 Paired-End 100bp S4 flowcell (Illumina, 20028313) with a final concentration of 300pM spiked with 1% PhiX control (Illumina, 15051973).

RNA-seq data processing

We used the DKFZ/ODCF workflows for RNAseq v1.3.0-0, Alignment and QC v1.2.73-3 (https://github.com/DKFZ-ODCF) deployed on the Roddy framework (Roddy v3.5.9; Default-Plugin v1.2.2-0; Base-Plugin v1.2.1-0; https://github.com/TheRoddyWMS/). Paired end FASTQ reads were aligned using the STAR aligner v2.5.3a (Dobin et al., 2013) by a 2-pass alignment. The reads were aligned to a STAR index generated from the 1000 genomes assembly, gencode 19 gene models (1KGRef_PhiX) and for a sjbdOverhang of 200. The alignment call parameters were --twopassMode Basic --twopass1readsN -1 --genomeLoad NoSharedMemory --outSAMtype BAM Unsorted SortedByCoordinate --limitBAMsortRAM 100000000000 --outBAMsortingThreadN=1 --outSAMstrandField intronMotif --outSAMunmapped Within KeepPairs --outFilterMultimapNmax 1 --outFilterMismatchNmax 5 --outFilterMismatchNoverLmax 0.3 --chimSegmentMin 15 --chimScoreMin 1 --chimScoreJunctionNonGTAG 0 --chimJunctionOverhangMin 15 --chimSegmentReadGapMax 3 --alignSJstitchMismatchNmax 5 -1 5 5 --alignIntronMax 1100000 --alignMatesGapMax 1100000 --alignSJDBoverhangMin 3 --alignIntronMin 20. Duplicate marking of the resultant main alignment files, as well as generating BAM indices was done with sambamba v0.6.5 (Tarasov et al., 2015). Quality control analysis was performed using the samtools flagstat command (samtools v1.6), and the rnaseqc tool (DeLuca et al., 2012).

Featurecounts from the subread package v1.6.5 was used to perform gene specific read counting over exon features based on the gencode 19 gene models (Liao et al., 2014). Strand unspecific

counting was used. Both reads of a paired fragment were used for counting and the quality threshold was set to 255.

Gene expression analysis and gene set testing

The raw RNA-seq counts were imported into R and saved as DGELists (Robinson and Oshlack, 2010). Genes with less than 10 counts across all samples were filtered followed by trimmed mean of M values (TMM) normalization (Robinson and Oshlack, 2010) and variance modeling using voom (Law et al., 2016). Batch effects were determined on the principal component analysis (PCA) projections and were corrected for by a linear regression model. Differential gene expression was performed using the limma RNA-seq pipeline (Law et al., 2016). Differentially regulated genes were considered significant at a p-value of less than or equal to 0.05. We retrieved the gene sets of the AHR-signature (Sadik et al., 2020) and autophagy regulators (Bordi et al., 2021) for gene set testing. Comparing the state of activity of any gene set was performed by a non-competitive gene set test using ROAST (Wu et al., 2010). Multiple testing correction was performed by applying the Benjamini-Hochberg procedure.

**TCGA glioblastoma expression data**

Data download

We downloaded and manually curated the metadata entries of 614 submitted glioblastoma patient samples. We excluded 42 entries that were either, duplicates, referring to normal tissue, control analytes, resected from the wrong site or of recurrent tumors. We selected the patient data generated on the two channel Agilent 244K Custom Gene Expression array because it was used for all remaining 572 samples. The Cy3 channel was hybridized with the Stratagene Universal RNA Reference and the Cy5 channel was hybridized with the sample. We used the unique identifiers to download the raw microarray data using GDC-client v1.1.0. (https://portal.gdc.cancer.gov/legacy-archive/search/f)

Data annotation

Two different versions of the custom array were used, G4502A-07-1 and G4502A-07-2. Both arrays had ~87% of common probes, which were later used to merge the patient data from both versions together. The array design files (ADF) and FASTA files were downloaded from https://www.cancer.gov/about-nci/organization/ccg/research/structural-genomics/tcga/using-tcga/technology). We created a new annotation file by aligning the 60 k-mer probes to the non-redundant nucleotide database (https://ftp.ncbi.nlm.nih.gov/blast/db/FASTA/nt.gz; reference build

hg38; downloaded on 21.07.2016) by using BLAST+ v2.2.30 and the following call parameters blastn -query unique.probes -task blastn -db nt -out resultblastn.txt -evalue 0.0001 -outfmt "6 std sgi nident staxids sscinames sstitle scomnames sstrand qcovhsp" -num_threads 14. The blast result was annotated using mygene v1.8 and additional gene information was added using the NCBI gene-info file (ftp://ftp.ncbi.nlm.nih.gov/gene/DATA/gene_info.gz; downloaded on 15.08.2016). The annotation file was filtered by removing all hits without the human taxid (9606), and with less than 60bp matching, a mismatch > 0, and without an “NM_” RefSeq accession prefix.

Data processing

We used the Sample and Data Relationship Format files (SDRF) to group the microarray data according to the chip version used. For each group the raw files were imported using the read.maimages function from the limma package. The probes of the raw matrix were background corrected using the “normexp” method with a setoff value of 50, followed by within array normalization using the LOESS-smoothing algorithm. Only probes that were successfully annotated as described above were retained. For every gene, probes were summarized into a single value (gene-set). If a gene was represented by more than three probes, we calculated the median absolute deviation (mad), and if a probe had a value outside the closed interval [-1.5, 1.5] mad, it was counted as an outlier and was filtered out. The remaining probes were averaged to represent the single gene value. All genes with 3 probes or less were averaged, and in the case of genes reported as a single probe, the single probe value was used. The resulting normalized matrix was saved into an MA-list object also including the curated meta- and clinical data. Finally, samples were filtered out if they had a reported IDH mutation, any missing clinical data, or of age below 30 years. The final MA-list comprised of 406 patients (GBM406).

Feature selection for identifying glioblastoma subgroups

We performed a feature selection step to identify glioblastoma patient subgroups showing high AHR expression and activity, while also reflecting the starvation phenotype observed in the LN-18 and LN-229 RNA-seq experiments. First, we compiled all differentially expressed genes from the topTables that had an average expression greater than or equal to 1 log2 counts per million, a log2 fold change of 0.58 or higher for upregulated genes and -0.58 or lower for downregulated genes, and adjusted p-value of at least 0.05. The genes fulfilling this criteria in those experiments were 2812 (starvation-features). Next, we estimated immune infiltration scores for the GBM406 patient dataset using the MCP-counter package v1.2.0 (Becht et al., 2016). Principle component analysis using the FactoMineR package v2.6 was performed with MCP-scores. The starvation-

features were correlated with the Eigenvalues of each of the first five principle components. Only 1628 genes were left after filtering all other genes that didn't have a correlation coefficient greater than or equal to 0.3 or less than or equal to -0.3,and a p-value of at least 0.05, with at least one of the first five principle components.

Defining glioblastoma subgroups

We applied a graph-based approach to identify glioblastoma subgroups. The subset of the expression matrix comprising the 1628 genes was used for identifying glioblastoma subgroups. First, we created a nearest neighbour graph using the cccd package v1.6. We used the correlation between the genes as a measure of distance, set the k-nearest neighbours to 10, and selected the kd-tree algorithm for the graph embedding (Arya and Mount, 1993; Arya et al., 1998; Bentley, 1975). We used the Louvain algorithm (Blondel et al., 2008) for community detection, which defined the seven GB subgroups.

Generating enrichment scores

Single sample enrichment scores for the AHR signature (Sadik et al., 2020) and autophagy regulators (Bordi et al., 2021) were generated using the GSVA package (Hanzelmann et al., 2013). In brief, this method accounts for biases resulting from the difference in GC content across genes. Using a Gaussian kernel the expression values were scaled by estimating the non-parametric kernel of its cumulative density function, which was used for estimating a rank distribution. Kolmogorov Smirnov like random walk statistic was used to calculate a normalized enrichment score based on the absolute difference of the magnitude of the positive and negative random walk deviations.

TCGA RPPA data

We downloaded level-4 normalized reverse phase protein arrays (RPPA) of TCGA glioblastoma patients from The Cancer Proteome Atlas (TCPA) (http://tcpaportal.org/tcpa). The data was subset of patients of the GBM406 dataset.

Interaction network analysis

Volcano plot representation of LN-18 RNA-seq dataset was performed using tidyverse package in Rstudio. A cut-off (|Log2FC| > 0.5 and adjusted P value < 0.05) was applied to count significantly altered genes. Autophagy-related genes that were upregulated upon Trp restriction were extracted by referencing a previous report (Bordi et al., 2021). The identified autophagy-related genes were

subjected to interaction network analysis using STRING database (Szklarczyk et al., 2021). Physical interaction networks were generated and subjected to k-means clustering (cluster n = 5) to obtain subnetworks, which were further classified based on their functions of components (Bordi et al., 2021).

**ATF4-AHR promoter binding**

The ATF4 binding site on the AHR promoter region was retrieved from the Transcription Factor Target Gene Database (http://tfbsdb.systemsbiology.net/) (Plaisier et al., 2016). ENCODE data indicative of the chromatin state were taken from the UCSC browser, including histone H3 lysine 27 acetylation (hg19, ENCODE histone modification tracks), DNase hypersensitivity cluster information (Integrated Regulation from ENCODE, V3) and chromatin segmentation states (Broad ChromHMM). The ATF4 binding site was visualized in conjunction with the ENCODE data.

**Protein isolation and immunoblot**

For protein harvest, cells were washed once with ice-cold PBS (Gibco, 14190169) and lysed with radio immunoprecipitation assay (RIPA) buffer containing 1% IGEPAL CA-630 (Sigma-Aldrich, I8896), 0.1% SDS (Carl Roth, 8029.3), and 0.5% sodium deoxycholate (AppliChem, A1531) in PBS supplemented with Phosphatase Inhibitor Cocktail 2 and Cocktail 3 (Sigma-Aldrich, P5726, P0044) and Complete Protease Inhibitor Cocktail (Roche, 11836145001) and centrifuged for 10 min at 13,000 g and 4°C. Protein concentration was determined using Protein Assay Dye Reagent Concentrate (Bio-Rad, 5000006), and absorbance was measured at 595 nm using a spectrophotometer (GE Healthcare). All samples within one experiment were adjusted to the lowest absorbance value. Cell lysates were mixed with 5x Laemmli buffer containing 10% glycerol (Sigma-Aldrich, 15523), 1% beta-mercaptoethanol (Sigma-Aldrich, M3148), 1.7% SDS (Carl Roth, 8029.3), 62.5 mM TRIS base (Sigma-Aldrich, T1503) [pH 6.8], and bromophenol blue (Sigma-Aldrich, B5525), and boiled for 5 min at 95ºC. Separation of proteins was performed with SDS polyacrylamide gel electrophoresis (PAGE) using gels with a concentration of 8%, 10%, 14% or 15% acrylamide (Carl Roth, 3029.1) in a Mini-PROTEAN Tetra Vertical Electrophoresis Cell system (Bio-Rad, 1658029FC) with running buffer containing 0.2 M glycine (Sigma-Aldrich, 33226), 25 mM TRIS base (Sigma-Aldrich, T1503), and 0.1% SDS (Carl Roth, 8029.3) at 80 - 150 V. Proteins were blotted onto a PVDF membrane (Merck Millipore, IPVH00010) or nitrocellulose membrane (Sigma-Aldrich, GE10600001) at 45 V for 2 h using the Mini-PROTEAN Tetra Vertical Electrophoresis Cell System (Bio-Rad, 1658029FC) and the blotting buffer containing 0.1 M glycine (Sigma-Aldrich, 33226), 50 mM TRIS base (Sigma-Aldrich, T1503), 0.01% SDS (Carl

Roth, 8029.3) [pH 8.3], and 10% methanol (Merck, 1.06009.2511). Membranes were blocked for 1 h at RT in 5% BSA (Carl Roth, 8076.5) in Tris-buffered saline tween (TBST) buffer (0.15 M NaCl (Sigma-Aldrich, S7653), 60 mM TRIS base (Sigma-Aldrich, T1503), 3 mM KCl (Sigma-Aldrich, P405), and 0.1% Tween-20 (Sigma-Aldrich, P9416), [pH 7.4]). Primary antibodies were diluted as recommended by the manufacturer in 5% BSA in TBST and incubated overnight at 4°C. On the next day, membranes were washed three times for 10 min in TBST buffer and subsequently incubated for 2 h with the respective horseradish peroxidase (HRP)-coupled secondary antibody dissolved in 5% BSA in TBST buffer. After another three 10 min wash steps in TBST buffer, proteins were detected using ECL Western Blotting Substrate (Thermo Fisher Scientific, 32106, Amersham, RPN2235), or SuperSignal West FEMTO (Thermo Fisher Scientific, 34096) under a ChemiDoc XRS+ camera system (Bio-Rad, 1708265) or a Fusion Fx camera (Vilber). Images taken with the ChemiDoc XRS+ were quantified with the Image Lab software (Bio-Rad, v6.0.1). Images taken with the Fusion FX camera were quantified with the ImageQuant TL 1D (v8.2.0). Normalization was performed as described (Prentzell et al., 2021). In brief, the images were first normalized by the pixel values of a single lane to the average value of all lanes in a blot for each antibody. Subsequently, the internally normalized proteins were normalized to the loading control glycerinaldehyd-3-phosphat-dehydrogenase (GAPDH), tubulin (TUBA1B), or vinculin (VCL), as indicated.

**Puromycin Assay**

Protein synthesis was measured by puromycin assay. Therefore, 5 µg/mL puromycin (Sigma-Aldrich, P8833) was added directly to the media 5 min prior lysis. Puromycin incorporation was detected by immunoblot analysis, as described above. The entire lane was used for quantification of the puromycin blots.

**Ras pull down assay**

For Ras pull down, 6.5 x $10^5$ LN-18 cells per 15 cm dish (TPP, 93150) were plated in phenol-red free complete DMEM (Gibco, 31053-028) supplemented with 2 mM L-glutamine (Lonza, 17-605E) and 1 mM sodium pyruvate (Gibco, 11360-039) and medium was changed after 24 h to phenol-red free customized Trp-free DMEM (Gibco, ME15175L1). Cells were starved for 24 h in the absence of Trp. Cells were collected in MLB buffer (RAS Activation Assay Kit, Merck Millipore, 17-218) after 30 min of 10 ng/mL EGF (Preprotech, AF-100-15) stimulation. Protein concentration

was determined using BCA assay (Thermo Fisher Scientific, 23227) and pellets were frozen in -80°C.

The RAS GTP pull-down assay was performed as described in Heberle et al, 2019 (Heberle et al., 2019). In short, 500 µL protein extracts (800 µg - 1 mg, adjusted depending on the lowest concentration in each replicate) were incubated for 45 min at 4°C with 10 µL agarose beads using a RAS-GTP pull-down assay kit (RAS Activation Assay Kit, Merck Millipore, 17-218). Supernatant was recovered after centrifugation, mixed with 40 µL of Laemmli buffer, incubated at 95°C for 5 min, centrifuged and stored at -20°C. For immunoblot analysis of RAS-GTP levels 20 µL of protein exctract was separated by gel electrophoresis, blotted and incubated overnight in 5% skim milk (GERBU Biotechnik, 70166) in TBST at 4°C with an anti-RAS antibody (Millipore, 05-516). As a loading control, glutathione-S transferase (GST; CST#2622) was tested in 5% skim milk in TBST for 2 h at RT. Immunoblots were quantified using ImageJ v.153k. Single lane chemiluminescence values were normalized to the average value of all lanes in a blot for each antibody, and subsequently normalized to the internal loading control GST.

**Immunofluorescence**

For immunofluorescence experiments, 1 x $10^5$ LN-18 cells were seeded per well into an 8-well IbiTreat µ-slide (Ibidi, 80826). Cells were cultured for 24 h in customized Trp-free DMEM (Gibco, ME15175L1) supplemented with 2 mM L-glutamine (Lonza, 17-605E) and 1 mM sodium pyruvate (Gibco, 11360-039) or cultured in Trp-containing complete DMEM (Gibco, 31053-028) as control. Cells were either stimulated with 10 ng/mL EGF for 15 min or medium was changed as control. Next, cells were washed with ice-cold PBS (Gibco, 14190169), fixed in 100% methanol (VWR, 85681-320) for 10 min at RT and permeabilized with 0.3% Triton X-100 (Sigma-Aldrich, T8787) in TBS for 10 min at 37°C. Prior to immunofluorescence, blocking was performed in TBS + 1% BSA (Carl Roth, 8076.5) for 2 h and incubated with anti-EGFR (CST, 4267, 1:200) and anti-LAMP2 (DSHB, H4B4; 1:200) antibodies for 3 h at RT. After three wash steps in TBS-T, anti-rabbit Alexa-488 (A-11008, Invitrogen, 1:500) and anti-mouse Alexa-647 antibodies (A-32728, Invitrogen, 1:1000) were added for 2 h at RT in the dark. Finally, nuclei were counterstained with 5 µg/mL DAPI (BD Biosciences, 564907) in TBS for 1 min.

Microscopy was performed using a CQ1 Confocal Quantitative Image Cytometer (Yokogawa Electric). For nuclear, EGFR focus and counting, binary masks were generated from intensity-thresholded images. For LAMP2 compartment size measurement, images were thresholded using an IJ_Isodata algorithm. The total measured area was normalized to nuclear count per image to

determine the mean LAMP2 compartment size per cell. Image analysis was performed using ImageJ v.153k.

**Macropinocytosis Assay**

For the uptake assay, 5 x $10^4$ LN-18 cells were seeded in 8-well IbiTreat µ-slides (Ibidi, 80826). On the next day, cells were washed with PBS (Gibco, 14190169) and cultivated for 24 h in 180 µL Trp-free or Trp-supplemented (78 µM) DMEM (Gibco, ME15175L1) medium with 2 mM L-glutamine. Subsequently, 20 µL of medium with 70 kDa-Dextran Oregon Green (dextran) (Invitrogen, D7173) with a final concentration of 0.1 mg/mL and 10 ng/mL EGF were added for 30 min. Next, cells were washed twice with ice-cold PBS and fixed with 4% formaldehyde (AppliChem, A3813) in PBS for 20 min at RT. Fixed cells were washed with PBS and incubated with 10 mg/mL DAPI (Serva Electrophoresis, 18860) in PBS for 10 min. Finally cells were washed again with PBS and imaged using an AxioObserver.Z1, equipped with an LSM780 ConfoCor 3 microscope with a 63x / 1.4 Oil DIC M27 Plan-Apochromat objective and ZEN 2012 (Zeiss, black edition, v8,1,0,484) software. Nuclear staining using DAPI was imaged with an UV diode (405 nm) and the dextran detection (488 nm) was performed using an argon multiline (458/488/514 nm). Detector gain and detector offset were adjusted once and never changed for an entire dataset. Raw images (CZI files) were subjected for further analyses in Fiji.

Dextran fluorescence was analyzed with Fiji version 1.52p using a background subtraction of 3, a Gaussian Blur filter of 1, threshold adjustment from 3500-max, a prominence of 10, and the ‘Analyze Particles’ function with a particle size from 5-infinity. The number (‘count’) of macropinosomes was then divided by the number of respective cells displayed in the DAPI channel in the analysed microscopy picture. The number of macropinosomes per cell were compared between at least 5 independent fields of view from 4 independent datasets. In total, between 27 and 29 independent fields of view were analyzed. For presentation in figures, ZEN 3.0 (Zeiss, blue edition) was used, and representative regions of interest for each condition were exported as TIFF with no compression using the ZEN ‘Best Fit’ option. Dextran green fluorescence was pseudo-colored white. Finally, brightness or contrast were adjusted for better visibility.

**Lysotracker**

For lysosome tracking, 5 x $10^4$ LN-18 cells were seeded in 8-well IbiTreat µ-slides (Ibidi, 80826). On the next day, cells were washed with PBS (Gibco, 14190169) and cultivated for 24 h in 200 µL Trp-free or Trp-supplemented (78 µM) DMEM (Gibco, ME15175L1) medium with 2 mM L-glutamine. 20 min before live cell imaging, cells were washed with PBS and 10 nM LysoTracker™

Red DND-99 (lysotracker) (Invitrogen, L7528) and 10 mg/mL DAPI (Serva Electrophoresis, 18860) in PBS were added. Living cells were imaged as above with an AxioObserver.Z1, equipped with an LSM780 ConfoCor 3 microscope with a 63x / 1.4 Oil DIC M27 Plan-Apochromat objective and ZEN 2012 (black edition, v8,1,0,484) software. Nuclear staining using DAPI was imaged with an UV diode (405 nm) and lysotracker with a 561 nm laser. Detector gain and detector offset were adjusted once and never changed for an entire dataset. Raw images (CZI files) were subjected for further analyses in Fiji. Lysotracker was analyzed with Fiji version 1.52p using a background subtraction of 3, a Gaussian Blur filter of 1, threshold adjustment from 3500-max, a prominence of 10, and the 'Analyze Particles' function with a particle size from 15-infinity. The raw integrated density (RawIntDen) value was then divided by the number of respective cells displayed in the DAPI channel in the analysed microscopy picture. The intensity of lysotracker foci per cell was then compared across at least 3 independent fields of view from 5 independent datasets. In total, between 24 and 28 independent fields of view were analysed.

**Simultaneous proteo-metabolome liquid-liquid extraction and measurement**

For the proteome analysis (**Figure 4F**), LN-18 cells were seeded in 10 cm plates containing complete DMEM (Biotech, P04-03600) supplemented with 2 mM L-glutamine (Gibco, 25030-024) at a density of 3 x $10^6$ cells per plate. The cells were cultured in the presence of 78 µM, 0.4, 0.2 or 0 µM Trp. After 24 h, the cells were washed three times with PBS. For proteome extraction, a simultaneous proteo-metabolome liquid-liquid extraction was used (van Pijkeren et al., 2022). The cell metabolism was quenched by addition of 500 µL ice-cold methanol (Fisher Chemical, 10653963) and 500 µL MS-grade water (Millipore, Direct Water Purification System). Lysates were scraped and transferred to tubes followed by the addition of 500 µL chloroform. After agitation in a cell shaker at 4°C for 20 min and 500 rpm, phase separation was performed by centrifugation at 4°C for 5 min at 16,100 g. Subsequently, after removing the liquid polar and non-polar phases, the solid interphases containing the proteomes were washed with methanol. Finally, interphases were dried, covered with 50 µL methanol, and stored at -80°C until further processing.

<u>Protein extraction from interphases</u>

To extract proteins, 60 µL of 8 M urea (Sigma-Aldrich, 51456) in 100 mM ammonium bicarbonate (Sigma-Aldrich, 09830-500G), pH 8.2 were added to the interphases followed by 240 µL of 100 mM $NH_4HCO_3$, pH 8.2. To bring proteins into solution, samples were sonicated with a tip sonicator (Thermo Fisher Scientific, 10588013). Protein concentration was determined using a microplate BCA protein assay kit (Thermo-Fisher-Scientific, 23227) following the manufacturer's instructions.

For protein determination, samples were diluted 1:50 in MilliQ water. A BSA standard was used to calibrate the assay across the concentration range of 0 - 200 µg/mL. The absorbance was measured at 580 nm using a plate reader (BMG Labtech, PHERAstar FSX). Extracts from samples that had been cultured with 0.4, 0.2 and 0 µM Trp were pooled.

Digestion and desalting

100 µg of dissolved protein was transferred into a new vial and filled to a final volume of 100 µL with the extraction buffer. Samples were incubated with 1 M DTT (Sigma-Aldrich, D0631) in 0.1 M triethylammonium bicarbonate (TEAB) (Sigma-Aldrich, 15715-58-9) to a final concentration of 10 mM DTT on a shaker for 30 min at 55°C and 800 rpm. Afterwards, alkylation was performed by 0.5 M iodoacetamide (IAA) (Sigma-Aldrich, I1149). IAA was added to a final concentration of 20 mM and incubated in the dark for 30 min. To quench the remaining IAA, DTT (1 M DTT in 0.1 M TEAB) was added. Digestion of the proteins was performed by the addition of trypsin (Gibco, 15400054) in a trypsin:protein ratio of 1:20. After overnight digestion at 37°C, the reaction was stopped by adding 100% formic acid (FA) (Fisher Scientific, 10596814) to achieve a final concentration of 1% FA in each sample.

Afterwards, peptide samples were desalted using Oasis HLB 1 cc Vac Cartridge (Waters, 186000383). For this, the cartridges were first activated with 1 mL of 100% methanol, followed by 1 mL of 95% ACN (Fisher Scientific, 10616653), 1% FA. Next, equilibration was performed by adding twice 1 mL of 1% FA. Peptide samples were slowly loaded onto the cartridge in 1 mL 1% FA. After washing twice with 1 mL 1% FA, samples were eluted from the cartridge with 1 mL 70% ACN, 1% FA. Samples were dried in a SpeedVac (Eppendorf, Concentrator 5301) and dried peptides were stored at -80°C until further processing.

LC-MS/MS analysis

For LC-MS/MS analysis, the dried tryptic peptides were dissolved in 20 µL 0.1% FA. The samples were injected on a nano-ultra pressure liquid chromatography system (Dionex UltiMate 3000 RSLCnano pro flow, Thermo Fisher Scientific) coupled via an electrospray ionization (ESI) source to an orbitrap hybrid mass spectrometer (QExactive, Thermo Scientific). The samples were loaded (5 µL/min) on a trapping column (nanoE MZ Sym C18, 5 µm, 180 µm x 20 mm, Waters; buffer A: 0.1% FA in HPLC-$H_2O$; buffer B: 100% ACN, 0.1% FA) with 100% buffer A. After sample loading, the trapping column was washed for 5 min with 100% buffer A (5 µL/min) and the peptides were eluted (300 nL/min) onto the separation column (nanoE MZ PST CSH, 130 A, C18, 1.7 µm, 75 µm x 250 mm, Waters) and separated with a gradient of 2−30% B in 60 min. The spray was generated from a steel emitter (Fisher Scientific) at a capillary voltage of 1850 V. MS/MS measurements were carried out in data dependent acquisition mode (DDA) using a normalized

HCD collision energy of 25% and a loop count of 15. MS scan was performed over an m/z range from 400-1200, with a resolution of 70,000 at m/z 200 (maximum injection time = 240 ms, AGC target = 1e6). MS/MS spectra were recorded over a m/z range of 200-2000 m/z with a resolution of 17,500 at m/z 200 (maximum injection time = 50 ms, maximum AGC target = 1e5, intensity threshold: 5e3), a quadrupole isolation width of 2 Da and an exclusion time of 20 seconds.

LC-MS/MS data processing

LC-MS/MS raw files were analysed with ProteomeDiscoverer 2.4 (Thermo Fisher Scientific). For peptide and protein identification, the LC-MS/MS were searched with SequesHT against a human database (SwissProt, 20,369 entries) and a contaminant database (116 entries). The following parameters were used for the data-base search: mass tolerance MS1: 10 ppm, mass tolerance MS2: 0.02 Da, fixed modification: carbamidomethylation (Cystein), variable modification: Oxidation (Methionine), variable modification at protein N-terminus: Acetylation, Methionine loss, Methionine loss + Acetylation. Percolator were used for FDR calculation. For feature detection, Minora Feature Detection was used with default settings. For label-free quantification, the Precursor Ions Quantifier was used with the following parameters: Peptides to use: unique peptides, Precursor Abundance Based On: Area, Minimum Replicate Features: 100%, Normalization Mode: Total Peptide Amount, Protein Abundance Calculation: Summed Abundances, Top N: 3, Hypothesis testing: t-test (Background Based). Adjusted p-values were calculated using Benjamini–Hochberg correction.

GO enrichment was performed with g:profiler (Raudvere et al., 2019). Resulting p-values were corrected with the Benjamini-Hochberg method. Visualization of results was done using the ggplot2 package in R (Wickham, 2016).

Extraction of intracellular Trp and quantificaction by mixed mode reversed phase-anion exchange UPLC-MS/MS

For amino acid analysis (**Figure 6P**), LN-18 cells were seeded in 6 cm plates containing complete DMEM (Biotech, P04-03600) supplemented with 2 mM L-glutamine (Gibco, 25030-024) at a density of $10^6$ cells per plate. The next day, cells were washed twice with PBS (Biotech, P04-36500) and Trp-containing (Gibco, 31053-028) or Trp-free DMEM (Gibco, ME15175L1) medium was added, each supplemented with 2 mM L-glutamine. 100 nM Bafilomycin A1 (MedChem Express, HY-100558) or the carrier DMSO (Sigma-Aldrich, D2650) were spiked into the medium 22 h later. 24 h after the medium exchange, the cells were treated as described in the Simultaneous proteo-metabolome liquid-liquid extraction paragraph. A fully $^{13}C$, $^{15}N$ labelled amino acid standard (Cambridge Isotope Laboratories, MSK-CAA-1) was spiked into samples at the first step of the extraction. Dried polar phases obtained from simultaneous extraction were dissolved

in 100 µL of water containing 5 mM ammonium formate ($NH_4FA$) (Sigma-Aldrich, 70221-100G-F) and 0.15% FA (Fisher Scientific, 10596814). 1 µL of each sample was injected. Analytes were separated at 40°C on an Atlantis Premier BEH C18 AX column (1.7 µm, 2.1 x 150 mm, Waters, 186009361) using an Acquity Premier UPLC system (Waters).

A gradient was run at a flowrate of 0.3 mL/min with mobile phase A (5 mM $NH_4FA$ and 0.15% FA in water) and mobile phase B (10 mM $NH_4FA$ and 0.15% FA 80% ACN) as follows: 5% B to 15% B in 2 min, 15% B to 70% B in 1.5 min, 70% B to 95% B in 0.5 min followed by 1 min of elution at 95% B and re-equilibration of the column to initial conditions over 2 min. Trp was detected using a Xevo-TQ XS Mass spectrometer (Waters) equipped with an electrospray ionization source running in positive mode. The transition from 205.1 -> 146.2 for endogenous Trp and 218.1 -> 156.1 were used for quantification. The cone voltage was set to 14 V and the collision energy was set to 18 V. Raw files were analysed in TargetLynx (Waters, V4.2 SCN1012). Resulting peak areas of endogenous and $^{13}C$, $^{15}N$ tryptophan were further analysed in R and resulting tryptophan concentrations were normalised to cell numbers.

Extraction of sphingolipids

For the measurement of sphingolipids (**Figure 7F**), LN-18 cells were seeded in 6 cm plates containing complete DMEM (Biotech, P04-03600) supplemented with 2 mM L-glutamine (Gibco, 25030-024) at a density of 1 x $10^6$ cells per plate. The next day, cells were washed twice with PBS (Biotech, P04-36500) and Trp-containing (Gibco, 31053-028) or Trp-free DMEM (Gibco, ME15175L1) medium was added, each supplemented with 2 mM L-glutamine. In addition, 1 µM of the AHR-inhibitor SR1 (Merck Millipore, 182706) or the carrier DMSO (Sigma-Aldrich, D2650) were spiked into the medium. The medium was removed after 24 h and cells were washed with 5 mL PBS (4°C). Cells were trypsinized with 1 mL 0.25% Trypsin-EDTA per dish (Gibco, 25200-056) for 5 min at 37°C and 5% CO2. After culture medium (4 ml) has been added, cells were pelleted (500 g, 5 min, 4°C), washed twice with ice-cold PBS (1.0 mL and 0.5 mL, 4°C), centrifuged (3000 g, 5 min, 4°C), frozen in liquid nitrogen, and stored at -80°C.

Sphingolipids were extracted from LN-18 cell pellets by successive addition of PBS pH 7.4, methanol, chloroform, and saline to a final ratio of 14:34:35:17 (Koeberle et al., 2010; Thurmer et al., 2022). The organic phase was evaporated to dryness using an Eppendorf Concentrator Plus System (Eppendorf, 5305000509; high vapor pressure application mode), and the remaining lipid film was dissolved in methanol, centrifuged twice at 21,100×g, 4°C for 5 min, and subjected to UPLC-MS/MS analysis. Internal standards used (Sigma-Aldrich): D-erythro-sphingosine-d7, N-heptadecanoyl-D-erythro-sphingosine, D-glucosyl-β-1,1′-N-heptadecanoyl-D-erythro-

sphingosine, N-lauroyl-ceramide-1-phosphate, N-heptadecanoyl-D-erythro-sphingosylphosphorylcholine, and D-erythro-sphingosine-d7-1-phosphate.

Analysis of sphingolipids by reversed phase UPLC-MS/MS

Chromatographic separation of sphingosines (Sph), (dihydro)ceramides ([dh]Cer), hexosylceramides (HexCer), ceramide-1-phosphates (C1P), and (dihydro)sphingomyelines ([dh]SM) was carried out at 45°C on an Acquity UPLC BEH C8 column (130Å, 1.7 µm, 2.1 × 100 mm, Waters, 186002878) using an ExionLC AD UHPLC system (Sciex). The gradient of mobile phase A (water/ACN, 90/10, 2 mM ammonium acetate) and mobile phase B (ACN/water, 95/5, 2 mM ammonium acetate) was ramped at a flow rate of 0.75 mL/min from 75% to 85% B within 5 min and to 100% B within another 2 min, followed by 13 min of isocratic elution.

Sphingolipids were analyzed in the positive ion mode by scheduled multiple reaction monitoring (MRM) using a QTRAP 6500$^+$ Mass Spectrometer (Sciex), which was equipped with an electrospray ionization source. Transitions from $[M+H]^+$ to $[M+H-H_2O]^+$ (Sph, dhCer), m/z = 184.1 ([dh]SM), and m/z = 264.4 (Cer, HexCer, C1P) were selected for quantitation. The curtain gas was set to 40 psi, the collision gas to medium, the ion spray voltage to 5000 V, the heated capillary temperature to 500°C, and the sheath and auxiliary gas pressure to 40 psi. The declustering potential was adjusted to 30 V (Sph, [dh]Cer, C1P) or 40 V (HexCer, [dh]SM), the entrance potential to 5 V (HexCer) or 10 V (Sph, [dh]Cer, C1P, [dh]SM), the collision energy to 20 eV (Sph), 30 eV ([dh]SM), 40 eV ([dh]Cer, C1P), or 50 eV (HexCer), and the collision cell exit potential to 5 V (C1P), 10 V ([dh]SM), 20 V ([dh]Cer, HexCer), or 25 V (Sph).

In variation to the procedure described above, sphingosine-1-phosphate (S1P) was separated on an Acquity UPLC CSH C18 column (130Å, 1.7 µm, 2.1 × 50 mm, Waters, 186005296) at 55°C. The LC system was operated at a flow rate of 0.55 mL/min using water/ACN (80/20) with 0.1% formic acid as mobile phase A and isopropanol/ACN (80/20) with 0.1% formic acid as mobile phase B. Initial conditions (60% B) were kept for 3 min, linearly increased to 70% B within 2 min and further to 100% B within 0.4 min, followed by isocratic elution for 1.6 min.

For the analysis of S1P in the positive ion mode ($[M+H]^+$) by MRM, $[M+H-H_3PO_4-H_2O]^+$ (m/z = 264.2) was detected as fragment ion. The curtain gas was set to 40 psi, the collision gas to low, the ion spray voltage to 4500 V, the heated capillary temperature to 500°C, the sheath gas pressure to 60 psi, the auxiliary gas pressure to 30 psi, the declustering potential to 40 V, the entrance potential to 10 V, the collision energy to 20 eV, and the collision cell exit potential to 20 V. Relative proportions of total ceramides (calculated as sum of ceramide species analysed) are

given as percentage of the sum of all sphingolipids determined in the corresponding sample (= 100%). Mass spectra were acquired and processed using Analyst 1.7.1 (Sciex) and Analyst 1.6.3 (Sciex), respectively.

**Ribosome Profiling**

For the ribosome profiling experiment, 6.5 x $10^4$ LN-229 cells/mL were seeded in 15 cm dishes (TPP, 93150) and were cultured on the next day 24 h in Trp-supplemented (78 µM) or Trp-free DMEM (Gibco, ME15175L1). Cells were washed with ice-cold PBS supplemented with 100 µg/mL CHX (Sigma Aldrich, C7698) and RP-Lysis buffer (20 mM Tris-HCL pH 7.5 (Thermo Fisher Scientific, 15567-027), 10 mM $MgCl_2$ (Sigma-Aldrich, M2393), 100 mM KCl (Sigma-Aldrich, P405), 1% Triton-X 100 (Sigma-Aldrich, T8787), 2 mM DTT (Sigma-Aldrich, D0631), 100 µg/mL CHX, 1x EDTA-free Complete Protease Inhibitor Cocktail (Sigma-Aldrich, 11873580001)) was added. After lysis, all samples were centrifuged at 6400 rpm, 4°C for 5 min. The supernatant was taken and digested with 1 U/µl RNaseI (Thermo Fisher Scientific, AM2295) for 45 min at RT under rotation. Digested lysates were run through 7% - 47% sucrose gradients using a Beckman Coulter ultracentrifuge and SW41 Ti rotor (Beckman Coulter) with 36,000 rpm at 4°C for 2 h. Monosome fractions were obtained and digested with 1% SDS (Sigma-Aldrich, 05030) and 0.113 µg/µL Proteinase K (Roche, 3115828001) for 45 min at 45°C. Resulting footprint RNA was extracted following a standard Phenol-Chloroform extraction (Zymo Research, R2050-1-200) and size-selected using a 10% denaturing PAGE gel.

RP library construction in brief: Footprint RNA was dephosphorylated using 5 U of T4 PNK (New England Biolabs, M0201S). Subsequently, preadenylated UMI-linkers were ligated to the RNA 3'end using 100 U T4 RNA Ligase 2, truncated K227Q (New England Biolabs, M0351L). Residual linker was eliminated by 25 U 5'Deadenylase and 15 U RecJf for 60 min at 30°C. Ribosomal RNA was substracted using a biotinylated rRNA oligo pool in 1x SSC buffer (3 M NaCl, 300 mM trisodium citrate, pH 7), which were pull down using MyOne Streptavidin C1 DynaBeads (Thermo Fisher Scientific, 65001). Resulting RNA footprints were reverse transcribed using the SuperScript III First-Strand Synthesis System (Thermo Fisher Scientific, 2232161). cDNA was size-selected using a 8% denaturing PAGE gel. cDNA was circularized by using the CircLigaseII Kit (Lucigen, CL9021K). The samples were subjected to PCR to introduce Illumina i7 indexes, followed by size-selection on an 8% non-denaturing PAGE gel. Resulting sample concentrations were measured with Qubit 3.0 (Thermo Fisher Scientific) using Qubit DNA HS kit (New England Biolabs, M0494S). The final RP libraries were single-end sequenced with a NextSeq2000 P2 system (Illumina).

RiboSeq data processing

All samples were sequenced at the DKFZ Sequencing Open Lab, associated with the DKFZ Genomics & Proteomics Core Facility. The FASTQ raw data was provided by the DKFZ Genomics & Proteomics Core Facility. In brief, sample adapters were trimmed using cutadapt (v3.4) (Martin, 2011) and demultiplexed with barcode_splitter from FASTX-toolkit (v0.0.6) (Gordon and Hannon, 2010). Fragments smaller than 30 nt were dropped. UMIs extraction was performed using umi_tools (v1.1.1) (Smith et al., 2017). By BLAST-Like Alignment Tool (BLAT) (v36x2), rRNA reads were filtered and discarded (Kent, 2002). The rRNA index for RNA18S5, RNA28S5 and RNA5-8S5 was constructed manually from NCBI RefSeq annotation. Remaining reads were aligned with Spliced Transcripts Alignment to a Reference (STAR) (v2.5.3a) (Dobin et al., 2013) to GRCh37/hg19 with `--outSAMtype BAM Unsorted --readFilesCommand zcat --quantMode TranscriptomeSAM GeneCounts --outSAMmapqUnique 0`. Following, PCR duplicates were removed using umi_tools. Genome browser bigwig tracks were obtained using samtools (v1.15.1) and bedtools (v2.24.0).

## STATISTICAL ANALYSIS

### Statistical analysis

GraphPad Prism (v9.4.1 or v8.4.3) was used for statistical analysis and statistical presentation unless otherwise specified. In case two conditions were compared, a paired or unpaired two-tailed Student's t-test was performed. If more than two conditions were compared, a one-way ANOVA followed by a Šídák's multiple comparisons test was applied. Immunoblot time courses with more than two conditions were compared using a two-way ANOVA followed by a Šídák's multiple comparisons test. For each experiment the number of replicates and the statistical test applied are indicated in the figure legend. Data are presented as mean ± SEM. *$p < 0.05$, **$p < 0.01$, ***$p < 0.001$, n.s.: not significant.

For bioinformatic analysis, unless otherwise stated, all pairwise comparisons were performed using Kruskal-Wallis and Wilcoxon sum rank tests, and all reported p-values were adjusted using the Benjamini-Hochberg procedure. All analyses were run in R, versions 3.3 and 4.2.2, (https://cran.r-project.org/) and Bioconductor version 3.3 and 3.15 (https://bioconductor.org/). All graphical representations were generated using ggplot2, ggpubr, gridExtra and RcolorBrewer.

## SUPPLEMENTAL INFORMATION

**Table S1**: qRT-PCR primers.

## REFERENCES

Adam, I., Dewi, D.L., Mooiweer, J., Sadik, A., Mohapatra, S.R., Berdel, B., Keil, M., Sonner, J.K., Thedieck, K., Rose, A.J., *et al.* (2018). Upregulation of tryptophanyl-tRNA synthethase adapts human cancer cells to nutritional stress caused by tryptophan degradation. Oncoimmunology *7*, e1486353.

Alesi, N., Akl, E.W., Khabibullin, D., Liu, H.J., Nidhiry, A.S., Garner, E.R., Filippakis, H., Lam, H.C., Shi, W., Viswanathan, S.R., *et al.* (2021). TSC2 regulates lysosome biogenesis via a non-canonical RAGC and TFEB-dependent mechanism. Nat Commun *12*, 4245.

Alesi, N., and Henske, E.P. (2022). Keeping up with the Rag GTPases. Nat Cell Biol *24*, 1330-1331.

Aquila, S., Santoro, M., Caputo, A., Panno, M.L., Pezzi, V., and De Amicis, F. (2020). The Tumor Suppressor PTEN as Molecular Switch Node Regulating Cell Metabolism and Autophagy: Implications in Immune System and Tumor Microenvironment. Cells *9*.

Arya, S., and Mount, D. (1993). Approximate nearest neighbor searching. Paper presented at: Proc 4th Ann ACMSIAM Symposium on Discrete Algorithms (SODA'93).

Arya, S., Mount, D.M., Netanyahu, N.S., Silverman, R., and Wu, A.Y. (1998). An optimal algorithm for approximate nearest neighbor searching fixed dimensions. Journal of the ACM (JACM) *45*, 891-923.

Badawy, A.A. (2018). Targeting tryptophan availability to tumors: the answer to immune escape? Immunol Cell Biol *96*, 1026-1034.

Barik, S. (2020). The Uniqueness of Tryptophan in Biology: Properties, Metabolism, Interactions and Localization in Proteins. Int J Mol Sci *21*.

Battaglioni, S., Benjamin, D., Walchli, M., Maier, T., and Hall, M.N. (2022). mTOR substrate phosphorylation in growth control. Cell *185*, 1814-1836.

Baumdick, M., Bruggemann, Y., Schmick, M., Xouri, G., Sabet, O., Davis, L., Chin, J.W., and Bastiaens, P.I. (2015). EGF-dependent re-routing of vesicular recycling switches spontaneous phosphorylation suppression to EGFR signaling. Elife *4*.

1520 Becht, E., Giraldo, N.A., Lacroix, L., Buttard, B., Elarouci, N., Petitprez, F., Selves, J., Laurent-
1521 Puig, P., Sautes-Fridman, C., Fridman, W.H.*, et al.* (2016). Estimating the population abundance
1522 of tissue-infiltrating immune and stromal cell populations using gene expression. Genome Biol
1523 *17*, 218.

1524 Ben-Sahra, I., Dirat, B., Laurent, K., Puissant, A., Auberger, P., Budanov, A., Tanti, J.F., and
1525 Bost, F. (2013). Sestrin2 integrates Akt and mTOR signaling to protect cells against energetic
1526 stress-induced death. Cell Death Differ *20*, 611-619.

1527 Ben-Sahra, I., Hoxhaj, G., Ricoult, S.J.H., Asara, J.M., and Manning, B.D. (2016). mTORC1
1528 induces purine synthesis through control of the mitochondrial tetrahydrofolate cycle. Science
1529 *351*, 728-733.

1530 Bentley, J.L. (1975). Multidimensional binary search trees used for associative searching.
1531 Communications of the ACM *18*, 509-517.

1532 Bi, J., Khan, A., Tang, J., Armando, A.M., Wu, S., Zhang, W., Gimple, R.C., Reed, A., Jing, H.,
1533 Koga, T.*, et al.* (2021). Targeting glioblastoma signaling and metabolism with a re-purposed
1534 brain-penetrant drug. Cell Rep *37*, 109957.

1535 Blondel, V.D., Guillaume, J.-L., Lambiotte, R., and Lefebvre, E. (2008). Fast unfolding of
1536 communities in large networks. Journal of statistical mechanics: theory and experiment *2008*,
1537 P10008.

1538 Bohm, R., Imseng, S., Jakob, R.P., Hall, M.N., Maier, T., and Hiller, S. (2021). The dynamic
1539 mechanism of 4E-BP1 recognition and phosphorylation by mTORC1. Mol Cell *81*, 2403-2416
1540 e2405.

1541 Bordi, M., De Cegli, R., Testa, B., Nixon, R.A., Ballabio, A., and Cecconi, F. (2021). A gene
1542 toolbox for monitoring autophagy transcription. Cell Death Dis *12*, 1044.

1543 Budanov, A.V., and Karin, M. (2008). p53 target genes sestrin1 and sestrin2 connect genotoxic
1544 stress and mTOR signaling. Cell *134*, 451-460.

1545 Champagne, J., Pataskar, A., Blommaert, N., Nagel, R., Wernaart, D., Ramalho, S., Kenski, J.,
1546 Bleijerveld, O.B., Zaal, E.A., Berkers, C.R.*, et al.* (2021). Oncogene-dependent sloppiness in
1547 mRNA translation. Mol Cell *81*, 4709-4721 e4709.

1548 Chen, R., Zou, Y., Mao, D., Sun, D., Gao, G., Shi, J., Liu, X., Zhu, C., Yang, M., Ye, W.*, et al.*
1549 (2014). The general amino acid control pathway regulates mTOR and autophagy during
1550 serum/glutamine starvation. J Cell Biol *206*, 173-182.

1551 Chresta, C.M., Davies, B.R., Hickson, I., Harding, T., Cosulich, S., Critchlow, S.E., Vincent, J.P.,
1552 Ellston, R., Jones, D., Sini, P.*, et al.* (2010). AZD8055 is a potent, selective, and orally
1553 bioavailable ATP-competitive mammalian target of rapamycin kinase inhibitor with in vitro and in
1554 vivo antitumor activity. Cancer Res *70*, 288-298.

1555 Colaprico, A., Silva, T.C., Olsen, C., Garofano, L., Cava, C., Garolini, D., Sabedot, T.S., Malta,
1556 T.M., Pagnotta, S.M., Castiglioni, I.*, et al.* (2016). TCGAbiolinks: an R/Bioconductor package for
1557 integrative analysis of TCGA data. Nucleic Acids Res *44*, e71.

1558 Compter, I., Eekers, D.B.P., Hoeben, A., Rouschop, K.M.A., Reymen, B., Ackermans, L.,
1559 Beckervordersantforth, J., Bauer, N.J.C., Anten, M.M., Wesseling, P.*, et al.* (2021). Chloroquine
1560 combined with concurrent radiotherapy and temozolomide for newly diagnosed glioblastoma: a
1561 phase IB trial. Autophagy *17*, 2604-2612.

1562 Deleyto-Seldas, N., and Efeyan, A. (2021). The mTOR-Autophagy Axis and the Control of
1563 Metabolism. Front Cell Dev Biol *9*, 655731.

1564 DeLuca, D.S., Levin, J.Z., Sivachenko, A., Fennell, T., Nazaire, M.D., Williams, C., Reich, M.,
1565 Winckler, W., and Getz, G. (2012). RNA-SeQC: RNA-seq metrics for quality control and process
1566 optimization. Bioinformatics *28*, 1530-1532.

1567 Deora, A.A., Win, T., Vanhaesebroeck, B., and Lander, H.M. (1998). A redox-triggered ras-
1568 effector interaction. Recruitment of phosphatidylinositol 3'-kinase to Ras by redox stress. J Biol
1569 Chem *273*, 29923-29928.

1570 Dikic, I. (2017). Proteasomal and Autophagic Degradation Systems. Annu Rev Biochem *86*, 193-
1571 224.

1572 Dobin, A., Davis, C.A., Schlesinger, F., Drenkow, J., Zaleski, C., Jha, S., Batut, P., Chaisson, M.,
1573 and Gingeras, T.R. (2013). STAR: ultrafast universal RNA-seq aligner. Bioinformatics *29*, 15-21.

1574 Dungo, R.T., and Keating, G.M. (2013). Afatinib: first global approval. Drugs *73*, 1503-1515.

1575 Ennis, H.L., and Lubin, M. (1964). Cycloheximide: Aspects of Inhibition of Protein Synthesis in
1576 Mammalian Cells. Science *146*, 1474-1476.

1577 Fabbri, L., Chakraborty, A., Robert, C., and Vagner, S. (2021). The plasticity of mRNA
1578 translation during cancer progression and therapy resistance. Nat Rev Cancer *21*, 558-577.

1579 Fallarino, F., Grohmann, U., You, S., McGrath, B.C., Cavener, D.R., Vacca, C., Orabona, C.,
1580 Bianchi, R., Belladonna, M.L., Volpi, C.*, et al.* (2006). The combined effects of tryptophan
1581 starvation and tryptophan catabolites down-regulate T cell receptor zeta-chain and induce a
1582 regulatory phenotype in naive T cells. J Immunol *176*, 6752-6761.

1583 Fernandes, S.A., and Demetriades, C. (2021). The Multifaceted Role of Nutrient Sensing and
1584 mTORC1 Signaling in Physiology and Aging. Front Aging *2*, 707372.

1585 Figlia, G., Muller, S., Hagenston, A.M., Kleber, S., Roiuk, M., Quast, J.P., Ten Bosch, N.,
1586 Carvajal Ibanez, D., Mauceri, D., Martin-Villalba, A.*, et al.* (2022). Brain-enriched RagB isoforms
1587 regulate the dynamics of mTORC1 activity through GATOR1 inhibition. Nat Cell Biol *24*, 1407-
1588 1421.

1589 Fiore, A., Zeitler, L., Russier, M., Gross, A., Hiller, M.K., Parker, J.L., Stier, L., Kocher, T.,
1590 Newstead, S., and Murray, P.J. (2022). Kynurenine importation by SLC7A11 propagates anti-
1591 ferroptotic signaling. Mol Cell *82*, 920-932 e927.

1592 Folkes, A.J., Ahmadi, K., Alderton, W.K., Alix, S., Baker, S.J., Box, G., Chuckowree, I.S., Clarke,
1593 P.A., Depledge, P., Eccles, S.A.*, et al.* (2008). The identification of 2-(1H-indazol-4-yl)-6-(4-
1594 methanesulfonyl-piperazin-1-ylmethyl)-4-morpholin-4-yl-t hieno[3,2-d]pyrimidine (GDC-0941) as
1595 a potent, selective, orally bioavailable inhibitor of class I PI3 kinase for the treatment of cancer. J
1596 Med Chem *51*, 5522-5532.

1597 Fukunaga, R., and Hunter, T. (1997). MNK1, a new MAP kinase-activated protein kinase,
1598 isolated by a novel expression screening method for identifying protein kinase substrates. EMBO
1599 J *16*, 1921-1933.

1600 Fumagalli, S., and Pende, M. (2022). S6 kinase 1 at the central node of cell size and ageing.
1601 Front Cell Dev Biol *10*, 949196.

1602 Gabriely, G., Wheeler, M.A., Takenaka, M.C., and Quintana, F.J. (2017). Role of AHR and HIF-
1603 1alpha in Glioblastoma Metabolism. Trends Endocrinol Metab *28*, 428-436.

1604 Gargaro, M., Manni, G., Scalisi, G., Puccetti, P., and Fallarino, F. (2021). Tryptophan
1605 Metabolites at the Crossroad of Immune-Cell Interaction via the Aryl Hydrocarbon Receptor:
1606 Implications for Tumor Immunotherapy. Int J Mol Sci *22*.

1607 Gibb, S., and Strimmer, K. (2012). MALDIquant: a versatile R package for the analysis of mass
1608 spectrometry data. Bioinformatics *28*, 2270-2271.

1609 Gingras, A.C., Gygi, S.P., Raught, B., Polakiewicz, R.D., Abraham, R.T., Hoekstra, M.F.,
1610 Aebersold, R., and Sonenberg, N. (1999). Regulation of 4E-BP1 phosphorylation: a novel two-
1611 step mechanism. Genes Dev *13*, 1422-1437.

1612 Gingras, A.C., Kennedy, S.G., O'Leary, M.A., Sonenberg, N., and Hay, N. (1998). 4E-BP1, a
1613 repressor of mRNA translation, is phosphorylated and inactivated by the Akt(PKB) signaling
1614 pathway. Genes Dev *12*, 502-513.

1615 Gingras, A.C., Raught, B., Gygi, S.P., Niedzwiecka, A., Miron, M., Burley, S.K., Polakiewicz,
1616 R.D., Wyslouch-Cieszynska, A., Aebersold, R., and Sonenberg, N. (2001). Hierarchical
1617 phosphorylation of the translation inhibitor 4E-BP1. Genes Dev *15*, 2852-2864.

1618 Golan-Lavi, R., Giacomelli, C., Fuks, G., Zeisel, A., Sonntag, J., Sinha, S., Kostler, W.,
1619 Wiemann, S., Korf, U., Yarden, Y.*, et al.* (2017). Coordinated Pulses of mRNA and of Protein
1620 Translation or Degradation Produce EGF-Induced Protein Bursts. Cell Rep *18*, 3129-3142.

1621 Gollwitzer, P., Grutzmacher, N., Wilhelm, S., Kummel, D., and Demetriades, C. (2022). A Rag
1622 GTPase dimer code defines the regulation of mTORC1 by amino acids. Nat Cell Biol *24*, 1394-
1623 1406.

1624 Gordon, A., and Hannon, G. (2010). Fastx-toolkit. FASTQ/A short-reads preprocessing tools
1625 (unpublished) http://hannonlab cshl edu/fastx_toolkit *5*.

1626 Grabocka, E., and Bar-Sagi, D. (2016). Mutant KRAS Enhances Tumor Cell Fitness by
1627 Upregulating Stress Granules. Cell *167*, 1803-1813 e1812.

1628 Guerrina, N., Aloufi, N., Shi, F., Prasade, K., Mehrotra, C., Traboulsi, H., Matthews, J.,
1629 Eidelman, D.H., Hamid, Q., and Baglole, C.J. (2021). The aryl hydrocarbon receptor reduces
1630 LC3II expression and controls endoplasmic reticulum stress. Am J Physiol Lung Cell Mol Physiol
1631 *320*, L339-L355.

1632 Guntaka, S.R., Samak, G., Seth, A., LaRusso, N.F., and Rao, R. (2011). Epidermal growth
1633 factor protects the apical junctional complexes from hydrogen peroxide in bile duct epithelium.
1634 Lab Invest *91*, 1396-1409.

1635 Hanzelmann, S., Castelo, R., and Guinney, J. (2013). GSVA: gene set variation analysis for
1636 microarray and RNA-seq data. BMC Bioinformatics *14*, 7.

1637 Haug, K., Cochrane, K., Nainala, V.C., Williams, M., Chang, J., Jayaseelan, K.V., and
1638 O'Donovan, C. (2020). MetaboLights: a resource evolving in response to the needs of its
1639 scientific community. Nucleic Acids Res *48*, D440-D444.

1640 Hay, N., and Sonenberg, N. (2004). Upstream and downstream of mTOR. Genes Dev *18*, 1926-
1641 1945.

1642 Heberle, A.M., Razquin Navas, P., Langelaar-Makkinje, M., Kasack, K., Sadik, A., Faessler, E.,
1643 Hahn, U., Marx-Stoelting, P., Opitz, C.A., Sers, C.*, et al.* (2019). The PI3K and MAPK/p38
1644 pathways control stress granule assembly in a hierarchical manner. Life Sci Alliance *2*.

1645 Hesketh, G.G., Papazotos, F., Pawling, J., Rajendran, D., Knight, J.D.R., Martinez, S., Taipale,
1646 M., Schramek, D., Dennis, J.W., and Gingras, A.C. (2020). The GATOR-Rag GTPase pathway
1647 inhibits mTORC1 activation by lysosome-derived amino acids. Science *370*, 351-356.

1648 Hosokawa, N., Hara, T., Kaizuka, T., Kishi, C., Takamura, A., Miura, Y., Iemura, S., Natsume,
1649 T., Takehana, K., Yamada, N.*, et al.* (2009). Nutrient-dependent mTORC1 association with the
1650 ULK1-Atg13-FIP200 complex required for autophagy. Mol Biol Cell *20*, 1981-1991.

1651 Hubbard, T.D., Murray, I.A., and Perdew, G.H. (2015). Indole and Tryptophan Metabolism:
1652 Endogenous and Dietary Routes to Ah Receptor Activation. Drug Metab Dispos *43*, 1522-1535.

1653 Inoki, K., and Guan, K.L. (2022). Rag GTPases regulate cellular amino acid homeostasis. Proc
1654 Natl Acad Sci U S A *119*.

1655 Jiang, Q., Li, F., Shi, K., Wu, P., An, J., Yang, Y., and Xu, C. (2013). ATF4 activation by the
1656 p38MAPK-eIF4E axis mediates apoptosis and autophagy induced by selenite in Jurkat cells.
1657 FEBS Lett *587*, 2420-2429.

1658 Kang, S.A., Pacold, M.E., Cervantes, C.L., Lim, D., Lou, H.J., Ottina, K., Gray, N.S., Turk, B.E.,
1659 Yaffe, M.B., and Sabatini, D.M. (2013). mTORC1 phosphorylation sites encode their sensitivity
1660 to starvation and rapamycin. Science *341*, 1236566.

1661 Kennedy, L.H., Sutter, C.H., Leon Carrion, S., Tran, Q.T., Bodreddigari, S., Kensicki, E.,
1662 Mohney, R.P., and Sutter, T.R. (2013). 2,3,7,8-Tetrachlorodibenzo-p-dioxin-mediated production
1663 of reactive oxygen species is an essential step in the mechanism of action to accelerate human
1664 keratinocyte differentiation. Toxicol Sci *132*, 235-249.

1665 Kent, W.J. (2002). BLAT--the BLAST-like alignment tool. Genome Res *12*, 656-664.

1666 Kilberg, M.S., Shan, J., and Su, N. (2009). ATF4-dependent transcription mediates signaling of
1667 amino acid limitation. Trends Endocrinol Metab *20*, 436-443.

1668 Kim, J., Kundu, M., Viollet, B., and Guan, K.L. (2011). AMPK and mTOR regulate autophagy
1669 through direct phosphorylation of Ulk1. Nat Cell Biol *13*, 132-141.

1670 Kim, Y.S., Ko, B., Kim, D.J., Tak, J., Han, C.Y., Cho, J.Y., Kim, W., and Kim, S.G. (2022).
1671 Induction of the hepatic aryl hydrocarbon receptor by alcohol dysregulates autophagy and
1672 phospholipid metabolism via PPP2R2D. Nat Commun *13*, 6080.

1673 Klaessens, S., Stroobant, V., De Plaen, E., and Van den Eynde, B.J. (2022). Systemic
1674 tryptophan homeostasis. Front Mol Biosci *9*, 897929.

1675 Klionsky, D.J., Abdel-Aziz, A.K., Abdelfatah, S., Abdellatif, M., Abdoli, A., Abel, S., Abeliovich,
1676 H., Abildgaard, M.H., Abudu, Y.P., Acevedo-Arozena, A.*, et al.* (2021). Guidelines for the use
1677 and interpretation of assays for monitoring autophagy (4th edition)(1). Autophagy *17*, 1-382.

1678 Klomp, J.E., Klomp, J.A., and Der, C.J. (2021). The ERK mitogen-activated protein kinase
1679 signaling network: the final frontier in RAS signal transduction. Biochem Soc Trans *49*, 253-267.

1680 Koeberle, A., Shindou, H., Harayama, T., and Shimizu, T. (2010). Role of lysophosphatidic acid
1681 acyltransferase 3 for the supply of highly polyunsaturated fatty acids in TM4 Sertoli cells. FASEB
1682 J *24*, 4929-4938.

1683 Konicek, B.W., Stephens, J.R., McNulty, A.M., Robichaud, N., Peery, R.B., Dumstorf, C.A.,
1684 Dowless, M.S., Iversen, P.W., Parsons, S., Ellis, K.E.*, et al.* (2011). Therapeutic inhibition of

1685 MAP kinase interacting kinase blocks eukaryotic initiation factor 4E phosphorylation and
1686 suppresses outgrowth of experimental lung metastases. Cancer Res *71*, 1849-1857.

1687 Kovalski, J.R., Kuzuoglu-Ozturk, D., and Ruggero, D. (2022). Protein synthesis control in cancer:
1688 selectivity and therapeutic targeting. EMBO J *41*, e109823.

1689 Kowalsky, A.H., Namkoong, S., Mettetal, E., Park, H.W., Kazyken, D., Fingar, D.C., and Lee,
1690 J.H. (2020). The GATOR2-mTORC2 axis mediates Sestrin2-induced AKT Ser/Thr kinase
1691 activation. J Biol Chem *295*, 1769-1780.

1692 Kumar, S., Sharife, H., Kreisel, T., Mogilevsky, M., Bar-Lev, L., Grunewald, M., Aizenshtein, E.,
1693 Karni, R., Paldor, I., Shlomi, T.*, et al.* (2019). Intra-Tumoral Metabolic Zonation and Resultant
1694 Phenotypic Diversification Are Dictated by Blood Vessel Proximity. Cell Metab *30*, 201-211
1695 e206.

1696 Law, C.W., Alhamdoosh, M., Su, S., Dong, X., Tian, L., Smyth, G.K., and Ritchie, M.E. (2016).
1697 RNA-seq analysis is easy as 1-2-3 with limma, Glimma and edgeR. F1000Res *5*.

1698 Lee, S., Rauch, J., and Kolch, W. (2020). Targeting MAPK Signaling in Cancer: Mechanisms of
1699 Drug Resistance and Sensitivity. Int J Mol Sci *21*.

1700 Lee, S.W., and Commisso, C. (2020). Rac1 and EGFR cooperate to activate Pak in response to
1701 nutrient stress. Biochem Biophys Res Commun *533*, 437-441.

1702 Lee, S.W., Zhang, Y., Jung, M., Cruz, N., Alas, B., and Commisso, C. (2019). EGFR-Pak
1703 Signaling Selectively Regulates Glutamine Deprivation-Induced Macropinocytosis. Dev Cell *50*,
1704 381-392 e385.

1705 Li, C., Hu, Y., Sturm, G., Wick, G., and Xu, Q. (2000). Ras/Rac-Dependent activation of p38
1706 mitogen-activated protein kinases in smooth muscle cells stimulated by cyclic strain stress.
1707 Arterioscler Thromb Vasc Biol *20*, E1-9.

1708 Li, K., Wada, S., Gosis, B.S., Thorsheim, C., Loose, P., and Arany, Z. (2022). Folliculin promotes
1709 substrate-selective mTORC1 activity by activating RagC to recruit TFE3. PLoS Biol *20*,
1710 e3001594.

1711 Liao, Y., Smyth, G.K., and Shi, W. (2014). featureCounts: an efficient general purpose program
1712 for assigning sequence reads to genomic features. Bioinformatics *30*, 923-930.

1713 Lin, B., Ziebro, J., Smithberger, E., Skinner, K.R., Zhao, E., Cloughesy, T.F., Binder, Z.A.,
1714 O'Rourke, D.M., Nathanson, D.A., Furnari, F.B.*, et al.* (2022). EGFR, the Lazarus target for
1715 precision oncology in glioblastoma. Neuro Oncol *24*, 2035-2062.

1716 Liu, G.Y., and Sabatini, D.M. (2020). mTOR at the nexus of nutrition, growth, ageing and
1717 disease. Nat Rev Mol Cell Biol *21*, 183-203.

1718 Liu, Q., Zhang, L., Allman, E.L., Hubbard, T.D., Murray, I.A., Hao, F., Tian, Y., Gui, W., Nichols,
1719 R.G., Smith, P.B.*, et al.* (2021). The aryl hydrocarbon receptor activates ceramide biosynthesis
1720 in mice contributing to hepatic lipogenesis. Toxicology *458*, 152831.

1721 Martin, M. (2011). Cutadapt removes adapter sequences from high-throughput sequencing
1722 reads. EMBnet journal *17*, 10-12.

1723 Martina, J.A., Chen, Y., Gucek, M., and Puertollano, R. (2012). MTORC1 functions as a
1724 transcriptional regulator of autophagy by preventing nuclear transport of TFEB. Autophagy *8*,
1725 903-914.

1726 Martinelli, E., Morgillo, F., Troiani, T., and Ciardiello, F. (2017). Cancer resistance to therapies
1727 against the EGFR-RAS-RAF pathway: The role of MEK. Cancer Treat Rev *53*, 61-69.

1728 Melick, C.H., and Jewell, J.L. (2020). Regulation of mTORC1 by Upstream Stimuli. Genes
1729 (Basel) *11*.

1730 Meng, D., Yang, Q., Wang, H., Melick, C.H., Navlani, R., Frank, A.R., and Jewell, J.L. (2020).
1731 Glutamine and asparagine activate mTORC1 independently of Rag GTPases. J Biol Chem *295*,
1732 2890-2899.

1733 Metz, R., Rust, S., Duhadaway, J.B., Mautino, M.R., Munn, D.H., Vahanian, N.N., Link, C.J., and
1734 Prendergast, G.C. (2012). IDO inhibits a tryptophan sufficiency signal that stimulates mTOR: A
1735 novel IDO effector pathway targeted by D-1-methyl-tryptophan. Oncoimmunology *1*, 1460-1468.

1736 Moerke, N.J., Aktas, H., Chen, H., Cantel, S., Reibarkh, M.Y., Fahmy, A., Gross, J.D., Degterev,
1737 A., Yuan, J., Chorev, M.*, et al.* (2007). Small-molecule inhibition of the interaction between the
1738 translation initiation factors eIF4E and eIF4G. Cell *128*, 257-267.

1739 Mulcahy Levy, J.M., and Thorburn, A. (2020). Autophagy in cancer: moving from understanding
1740 mechanism to improving therapy responses in patients. Cell Death Differ *27*, 843-857.

1741 Munn, D.H., Sharma, M.D., Baban, B., Harding, H.P., Zhang, Y., Ron, D., and Mellor, A.L.
1742 (2005). GCN2 kinase in T cells mediates proliferative arrest and anergy induction in response to
1743 indoleamine 2,3-dioxygenase. Immunity *22*, 633-642.

1744 Musa, J., Orth, M.F., Dallmayer, M., Baldauf, M., Pardo, C., Rotblat, B., Kirchner, T., Leprivier,
1745 G., and Grunewald, T.G. (2016). Eukaryotic initiation factor 4E-binding protein 1 (4E-BP1): a
1746 master regulator of mRNA translation involved in tumorigenesis. Oncogene *35*, 4675-4688.

1747 Nakase, I., Kobayashi, N.B., Takatani-Nakase, T., and Yoshida, T. (2015). Active
1748 macropinocytosis induction by stimulation of epidermal growth factor receptor and oncogenic
1749 Ras expression potentiates cellular uptake efficacy of exosomes. Sci Rep *5*, 10300.

1750 Napolitano, G., Di Malta, C., Esposito, A., de Araujo, M.E.G., Pece, S., Bertalot, G., Matarese,
1751 M., Benedetti, V., Zampelli, A., Stasyk, T.*, et al.* (2020). A substrate-specific mTORC1 pathway
1752 underlies Birt-Hogg-Dube syndrome. Nature *585*, 597-602.

1753 Norman, K.L., Hirasawa, K., Yang, A.D., Shields, M.A., and Lee, P.W. (2004). Reovirus
1754 oncolysis: the Ras/RalGEF/p38 pathway dictates host cell permissiveness to reovirus infection.
1755 Proc Natl Acad Sci U S A *101*, 11099-11104.

1756 Ogretmen, B. (2018). Sphingolipid metabolism in cancer signalling and therapy. Nat Rev Cancer
1757 *18*, 33-50.

1758 Opitz, C.A., Litzenburger, U.M., Sahm, F., Ott, M., Tritschler, I., Trump, S., Schumacher, T.,
1759 Jestaedt, L., Schrenk, D., Weller, M.*, et al.* (2011). An endogenous tumour-promoting ligand of
1760 the human aryl hydrocarbon receptor. Nature *478*, 197-203.

1761 Opitz, C.A., Somarribas Patterson, L.F., Mohapatra, S.R., Dewi, D.L., Sadik, A., Platten, M., and
1762 Trump, S. (2020). The therapeutic potential of targeting tryptophan catabolism in cancer. Br J
1763 Cancer *122*, 30-44.

1764 Palm, W., Park, Y., Wright, K., Pavlova, N.N., Tuveson, D.A., and Thompson, C.B. (2015). The
1765 Utilization of Extracellular Proteins as Nutrients Is Suppressed by mTORC1. Cell *162*, 259-270.

1766 Panitz, V., Koncarevic, S., Sadik, A., Friedel, D., Bausbacher, T., Trump, S., Farztdinov, V.,
1767 Schulz, S., Sievers, P., Schmidt, S.*, et al.* (2021). Tryptophan metabolism is inversely regulated
1768 in the tumor and blood of patients with glioblastoma. Theranostics *11*, 9217-9233.

1769 Pataskar, A., Champagne, J., Nagel, R., Kenski, J., Laos, M., Michaux, J., Pak, H.S., Bleijerveld,
1770 O.B., Mordente, K., Navarro, J.M.*, et al.* (2022). Tryptophan depletion results in tryptophan-to-
1771 phenylalanine substitutants. Nature *603*, 721-727.

1772 Pearson, J.R.D., and Regad, T. (2017). Targeting cellular pathways in glioblastoma multiforme.
1773 Signal Transduct Target Ther *2*, 17040.

1774 Perez-Riverol, Y., Bai, J., Bandla, C., Garcia-Seisdedos, D., Hewapathirana, S.,
1775 Kamatchinathan, S., Kundu, D.J., Prakash, A., Frericks-Zipper, A., Eisenacher, M.*, et al.* (2022).
1776 The PRIDE database resources in 2022: a hub for mass spectrometry-based proteomics
1777 evidences. Nucleic Acids Res *50*, D543-D552.

1778 Plaisier, C.L., O'Brien, S., Bernard, B., Reynolds, S., Simon, Z., Toledo, C.M., Ding, Y., Reiss,
1779 D.J., Paddison, P.J., and Baliga, N.S. (2016). Causal Mechanistic Regulatory Network for
1780 Glioblastoma Deciphered Using Systems Genetics Network Analysis. Cell Syst *3*, 172-186.

1781 Platten, M., Friedrich, M., Wainwright, D.A., Panitz, V., and Opitz, C.A. (2021). Tryptophan
1782 metabolism in brain tumors - IDO and beyond. Curr Opin Immunol *70*, 57-66.

1783 Prentzell, M.T., Rehbein, U., Cadena Sandoval, M., De Meulemeester, A.S., Baumeister, R.,
1784 Brohee, L., Berdel, B., Bockwoldt, M., Carroll, B., Chowdhury, S.R.*, et al.* (2021). G3BPs tether
1785 the TSC complex to lysosomes and suppress mTORC1 signaling. Cell *184*, 655-674 e627.

1786 Psychogios, N., Hau, D.D., Peng, J., Guo, A.C., Mandal, R., Bouatra, S., Sinelnikov, I.,
1787 Krishnamurthy, R., Eisner, R., Gautam, B.*, et al.* (2011). The human serum metabolome. PLoS
1788 One *6*, e16957.

1789 Puccini, J., Badgley, M.A., and Bar-Sagi, D. (2022). Exploiting cancer's drinking problem:
1790 regulation and therapeutic potential of macropinocytosis. Trends Cancer *8*, 54-64.

1791 Rabanal-Ruiz, Y., Otten, E.G., and Korolchuk, V.I. (2017). mTORC1 as the main gateway to
1792 autophagy. Essays Biochem *61*, 565-584.

1793 Raudvere, U., Kolberg, L., Kuzmin, I., Arak, T., Adler, P., Peterson, H., and Vilo, J. (2019).
1794 g:Profiler: a web server for functional enrichment analysis and conversions of gene lists (2019
1795 update). Nucleic Acids Res *47*, W191-W198.

1796 Riese, D.J., 2nd, and Cullum, R.L. (2014). Epiregulin: roles in normal physiology and cancer.
1797 Semin Cell Dev Biol *28*, 49-56.

1798 Roberts, P.J., and Der, C.J. (2007). Targeting the Raf-MEK-ERK mitogen-activated protein
1799 kinase cascade for the treatment of cancer. Oncogene *26*, 3291-3310.

1800 Robinson, M.D., and Oshlack, A. (2010). A scaling normalization method for differential
1801 expression analysis of RNA-seq data. Genome Biol *11*, R25.

1802 Rothhammer, V., and Quintana, F.J. (2019). The aryl hydrocarbon receptor: an environmental
1803 sensor integrating immune responses in health and disease. Nat Rev Immunol *19*, 184-197.

1804 Rouse, J., Cohen, P., Trigon, S., Morange, M., Alonso-Llamazares, A., Zamanillo, D., Hunt, T.,
1805 and Nebreda, A.R. (1994). A novel kinase cascade triggered by stress and heat shock that
1806 stimulates MAPKAP kinase-2 and phosphorylation of the small heat shock proteins. Cell *78*,
1807 1027-1037.

1808 Roux, P.P., and Topisirovic, I. (2018). Signaling Pathways Involved in the Regulation of mRNA
1809 Translation. Mol Cell Biol *38*.

1810 Russell, R.C., and Guan, K.L. (2022). The multifaceted role of autophagy in cancer. EMBO J *41*,
1811 e110031.

1812 Sadik, A., Somarribas Patterson, L.F., Ozturk, S., Mohapatra, S.R., Panitz, V., Secker, P.F.,
1813 Pfander, P., Loth, S., Salem, H., Prentzell, M.T.*, et al.* (2020). IL4I1 Is a Metabolic Immune
1814 Checkpoint that Activates the AHR and Promotes Tumor Progression. Cell *182*, 1252-1270
1815 e1234.

1816 Sammour, D.A., Cairns, J.L., Boskamp, T., Kessler, T., Guevara, C.R., Panitz, V., Sadik, A.,
1817 Cordes, J., Marsching, C., and Friedrich, M. (2021). Spatial Probabilistic Mapping of Metabolite
1818 Ensembles in Mass Spectrometry Imaging. bioRxiv.

1819 Saxton, R.A., Knockenhauer, K.E., Wolfson, R.L., Chantranupong, L., Pacold, M.E., Wang, T.,
1820 Schwartz, T.U., and Sabatini, D.M. (2016). Structural basis for leucine sensing by the Sestrin2-
1821 mTORC1 pathway. Science *351*, 53-58.

1822 Schalm, S.S., Fingar, D.C., Sabatini, D.M., and Blenis, J. (2003). TOS motif-mediated raptor
1823 binding regulates 4E-BP1 multisite phosphorylation and function. Curr Biol *13*, 797-806.

1824 Sekiyama, N., Arthanari, H., Papadopoulos, E., Rodriguez-Mias, R.A., Wagner, G., and Leger-
1825 Abraham, M. (2015). Molecular mechanism of the dual activity of 4EGI-1: Dissociating eIF4G
1826 from eIF4E but stabilizing the binding of unphosphorylated 4E-BP1. Proc Natl Acad Sci U S A
1827 *112*, E4036-4045.

1828 Shepherd, F.A., Rodrigues Pereira, J., Ciuleanu, T., Tan, E.H., Hirsh, V., Thongprasert, S.,
1829 Campos, D., Maoleekoonpiroj, S., Smylie, M., Martins, R.*, et al.* (2005). Erlotinib in previously
1830 treated non-small-cell lung cancer. N Engl J Med *353*, 123-132.

1831 Shinde, R., and McGaha, T.L. (2018). The Aryl Hydrocarbon Receptor: Connecting Immunity to
1832 the Microenvironment. Trends Immunol *39*, 1005-1020.

1833 Smith, T., Heger, A., and Sudbery, I. (2017). UMI-tools: modeling sequencing errors in Unique
1834 Molecular Identifiers to improve quantification accuracy. Genome Res *27*, 491-499.

1835 Sriram, A., Bohlen, J., and Teleman, A.A. (2018). Translation acrobatics: how cancer cells
1836 exploit alternate modes of translational initiation. EMBO Rep *19*.

1837 Sun, L. (2021). Recent advances in the development of AHR antagonists in immuno-oncology.
1838 RSC Med Chem *12*, 902-914.

1839 Tang, X., Liu, B., Wang, X., Yu, Q., and Fang, R. (2018). Epidermal Growth Factor, through
1840 Alleviating Oxidative Stress, Protect IPEC-J2 Cells from Lipopolysaccharides-Induced
1841 Apoptosis. Int J Mol Sci *19*.

1842 Tarasov, A., Vilella, A.J., Cuppen, E., Nijman, I.J., and Prins, P. (2015). Sambamba: fast
1843 processing of NGS alignment formats. Bioinformatics *31*, 2032-2034.

1844 Tate, C.M., Blosser, W., Wyss, L., Evans, G., Xue, Q., Pan, Y., and Stancato, L. (2013).
1845 LY2228820 dimesylate, a selective inhibitor of p38 mitogen-activated protein kinase, reduces
1846 angiogenic endothelial cord formation in vitro and in vivo. J Biol Chem *288*, 6743-6753.

1847 Thurmer, M., Gollowitzer, A., Pein, H., Neukirch, K., Gelmez, E., Waltl, L., Wielsch, N., Winkler,
1848 R., Loser, K., Grander, J.*, et al.* (2022). PI(18:1/18:1) is a SCD1-derived lipokine that limits
1849 stress signaling. Nat Commun *13*, 2982.

1850 Torrence, M.E., MacArthur, M.R., Hosios, A.M., Valvezan, A.J., Asara, J.M., Mitchell, J.R., and
1851 Manning, B.D. (2021). The mTORC1-mediated activation of ATF4 promotes protein and
1852 glutathione synthesis downstream of growth signals. Elife *10*.

1853 Valvezan, A.J., and Manning, B.D. (2019). Molecular logic of mTORC1 signalling as a metabolic
1854 rheostat. Nat Metab *1*, 321-333.

1855 van Pijkeren, A., Egger, A., Hotze, M., Zimmermann, E., Grander, J., Gollowitzer, A., Koeberle,
1856 A., Bischoff, R., Thedieck, K., and Kwiatkowski, M. (2022). Proteome coverage after
1857 simultaneous proteo-metabolome liquid-liquid extraction. bioRxiv, 2022.2007.2018.500507.

1858 Velasquez, C., Cheng, E., Shuda, M., Lee-Oesterreich, P.J., Pogge von Strandmann, L.,
1859 Gritsenko, M.A., Jacobs, J.M., Moore, P.S., and Chang, Y. (2016). Mitotic protein kinase CDK1
1860 phosphorylation of mRNA translation regulator 4E-BP1 Ser83 may contribute to cell
1861 transformation. Proc Natl Acad Sci U S A *113*, 8466-8471.

1862 Waskiewicz, A.J., Flynn, A., Proud, C.G., and Cooper, J.A. (1997). Mitogen-activated protein
1863 kinases activate the serine/threonine kinases Mnk1 and Mnk2. EMBO J *16*, 1909-1920.

1864 Wickham, H. (2016). ggplot2: Elegant Graphics for Data Analysis, 1 edn (Springer-Verlag New
1865 York).

1866 Wolfson, R.L., Chantranupong, L., Saxton, R.A., Shen, K., Scaria, S.M., Cantor, J.R., and
1867 Sabatini, D.M. (2016). Sestrin2 is a leucine sensor for the mTORC1 pathway. Science *351*, 43-
1868 48.

1869 Wu, D., Lim, E., Vaillant, F., Asselin-Labat, M.L., Visvader, J.E., and Smyth, G.K. (2010).
1870 ROAST: rotation gene set tests for complex microarray experiments. Bioinformatics *26*, 2176-
1871 2182.

1872 Yeh, T.C., Marsh, V., Bernat, B.A., Ballard, J., Colwell, H., Evans, R.J., Parry, J., Smith, D.,
1873 Brandhuber, B.J., Gross, S.*, et al.* (2007). Biological characterization of ARRY-142886
1874 (AZD6244), a potent, highly selective mitogen-activated protein kinase kinase 1/2 inhibitor. Clin
1875 Cancer Res *13*, 1576-1583.

1876 Yoshizawa, A., Fukuoka, J., Shimizu, S., Shilo, K., Franks, T.J., Hewitt, S.M., Fujii, T., Cordon-
1877 Cardo, C., Jen, J., and Travis, W.D. (2010). Overexpression of phospho-eIF4E is associated
1878 with survival through AKT pathway in non-small cell lung cancer. Clin Cancer Res *16*, 240-248.

1879 Zhai, L., Dey, M., Lauing, K.L., Gritsina, G., Kaur, R., Lukas, R.V., Nicholas, M.K., Rademaker,
1880 A.W., Dostal, C.R., McCusker, R.H.*, et al.* (2015). The kynurenine to tryptophan ratio as a
1881 prognostic tool for glioblastoma patients enrolling in immunotherapy. J Clin Neurosci *22*, 1964-
1882 1968.

1883

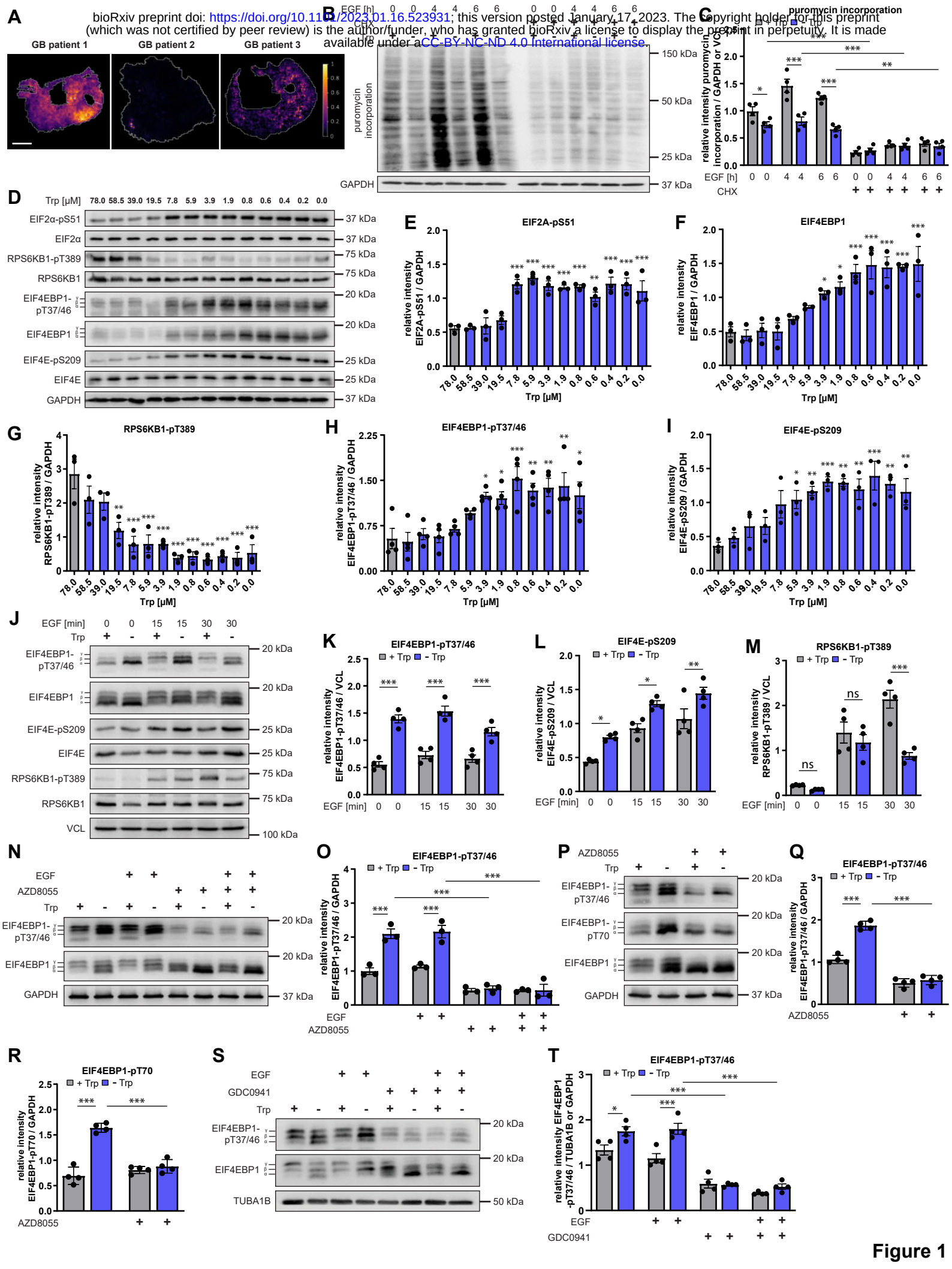


**Figure 1**

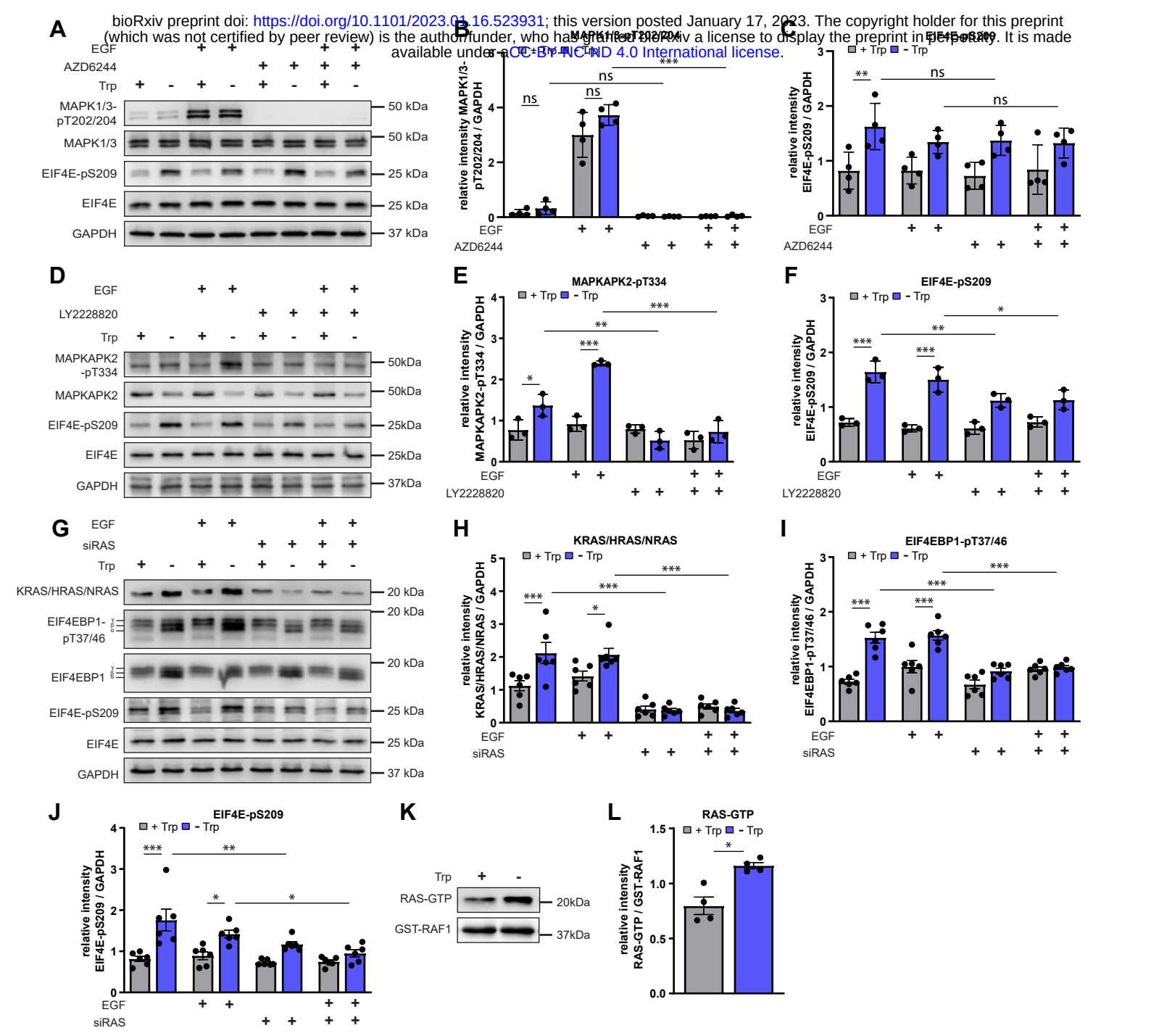


**Figure 2**

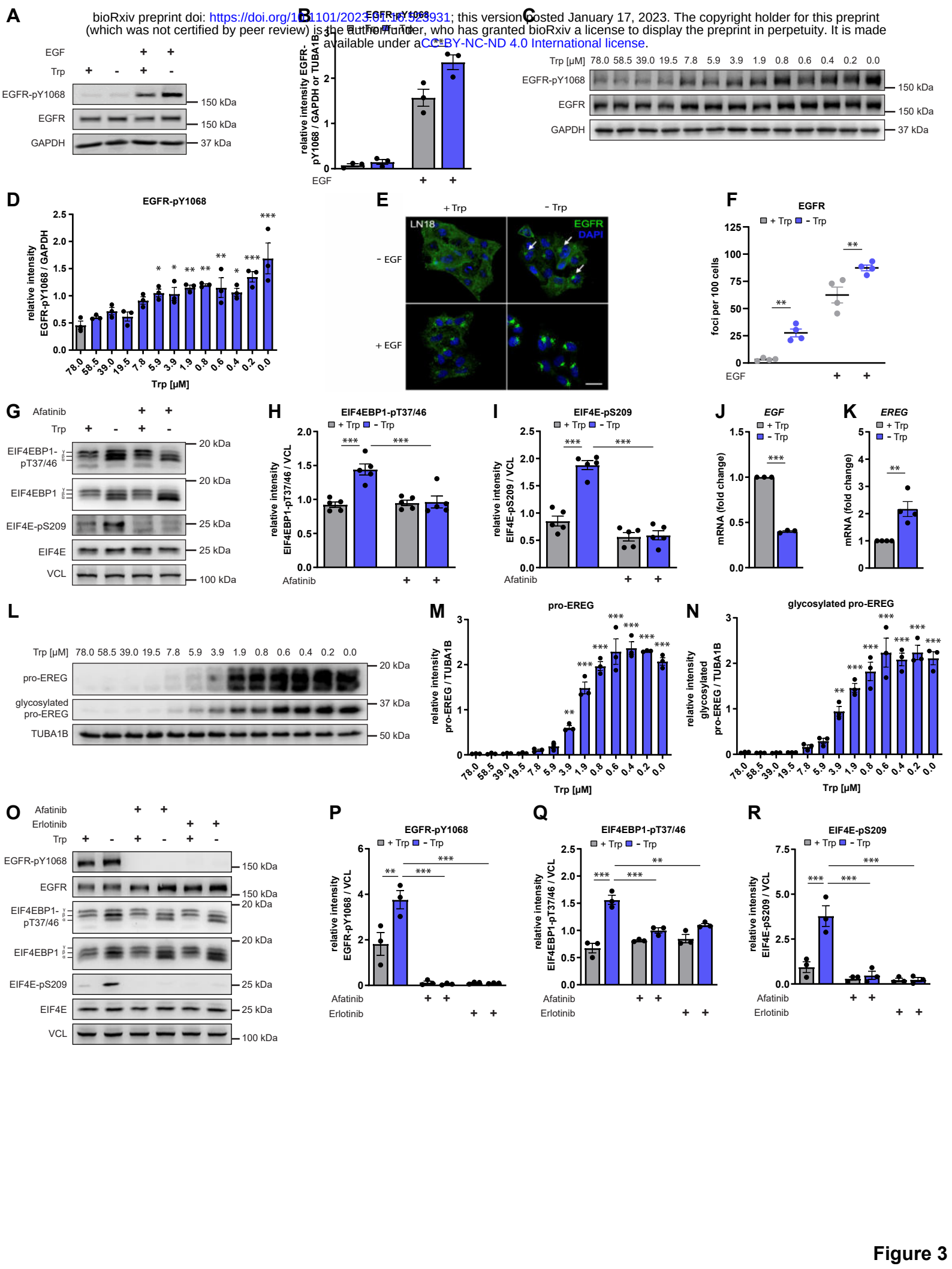


**Figure 3**

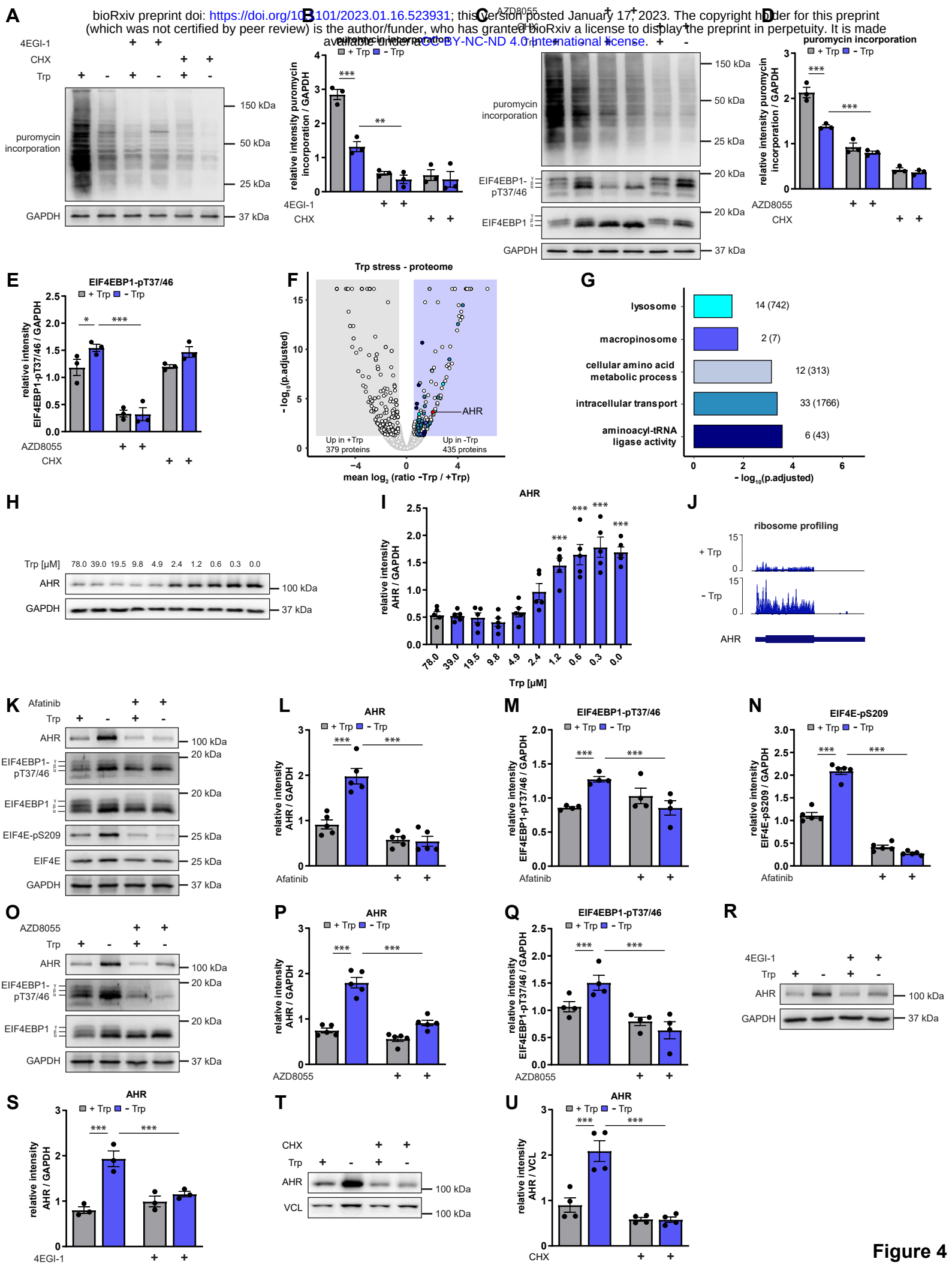


**Figure 4**

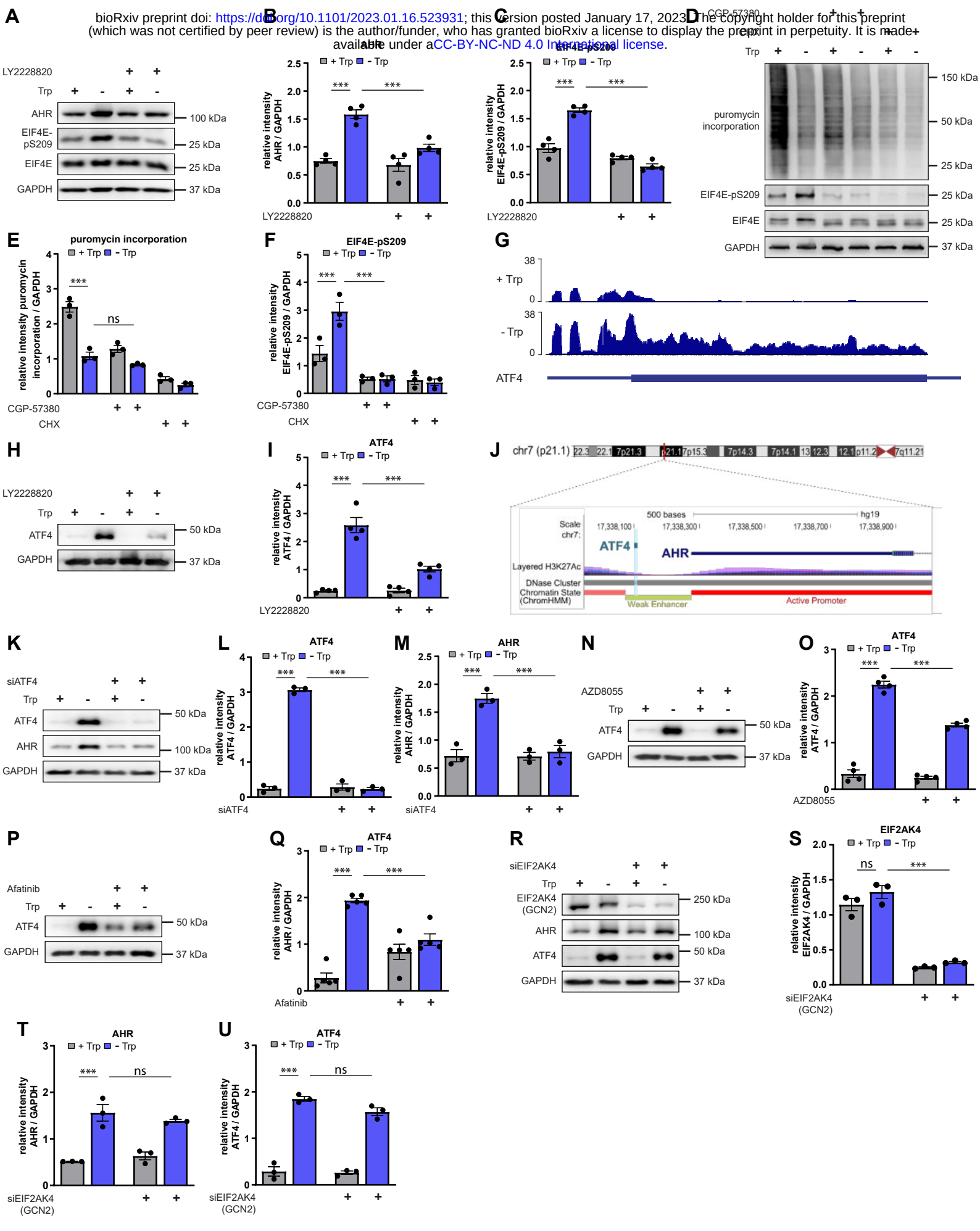


Figure 5

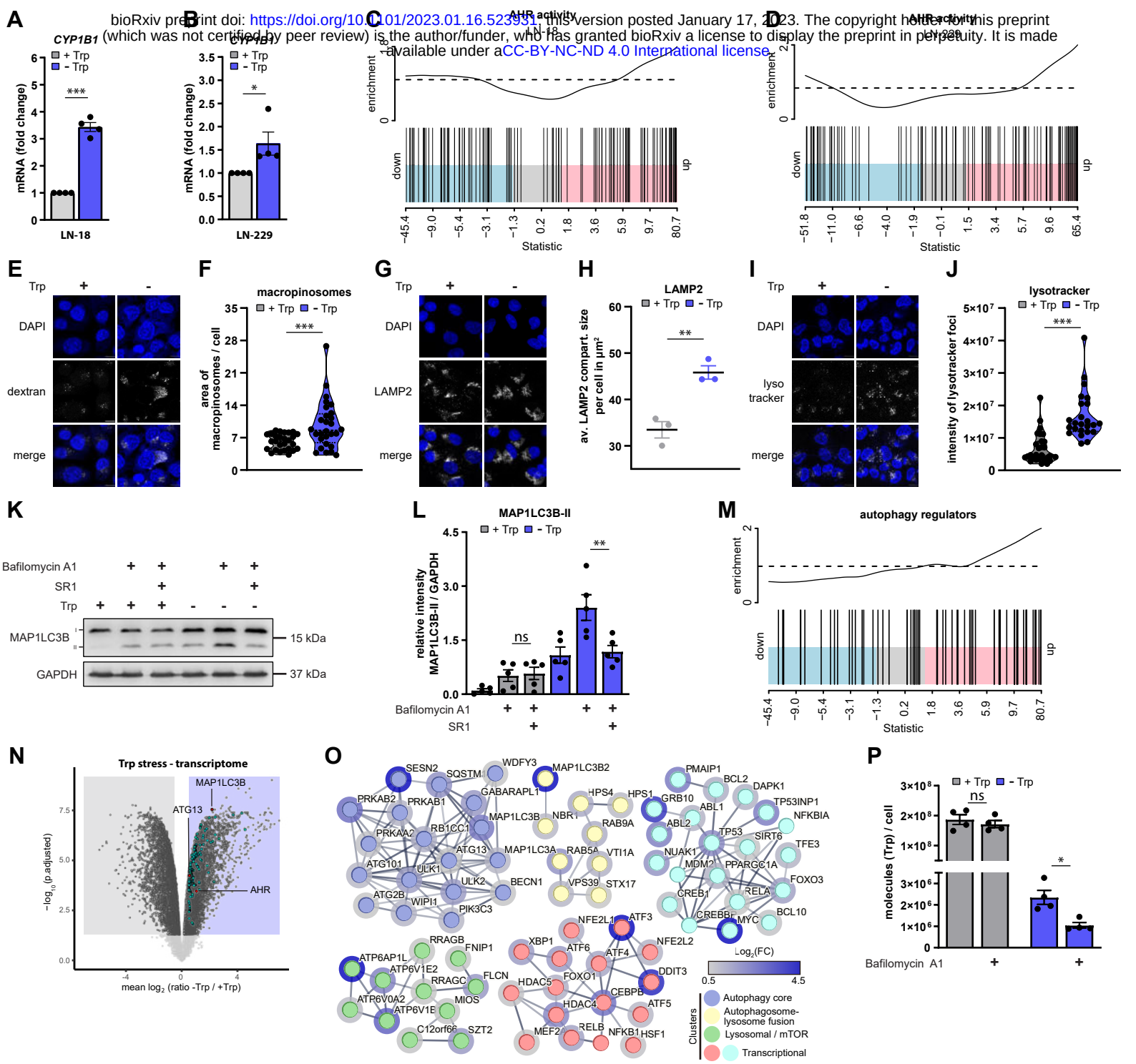


Figure 6

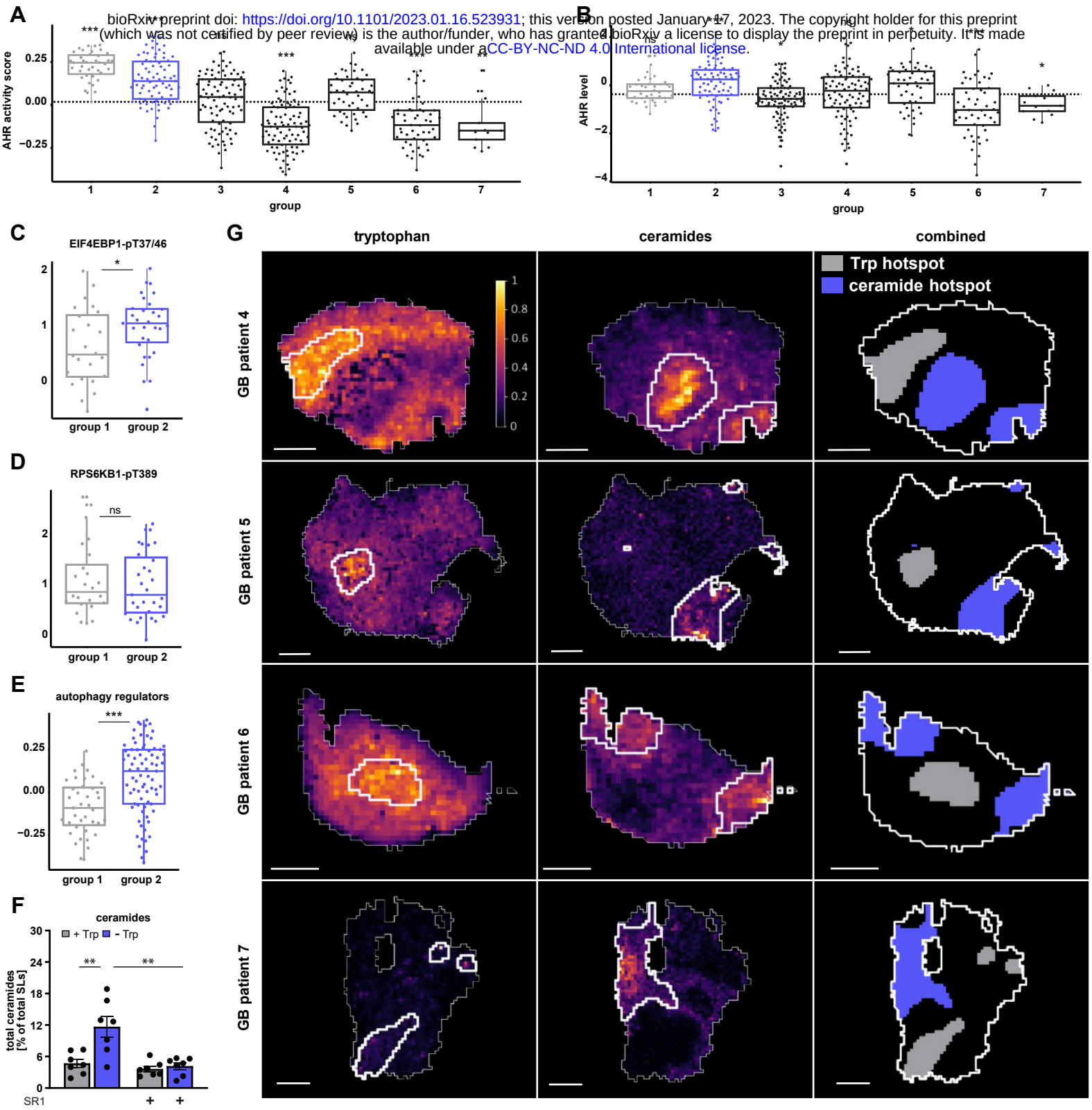


Figure 7

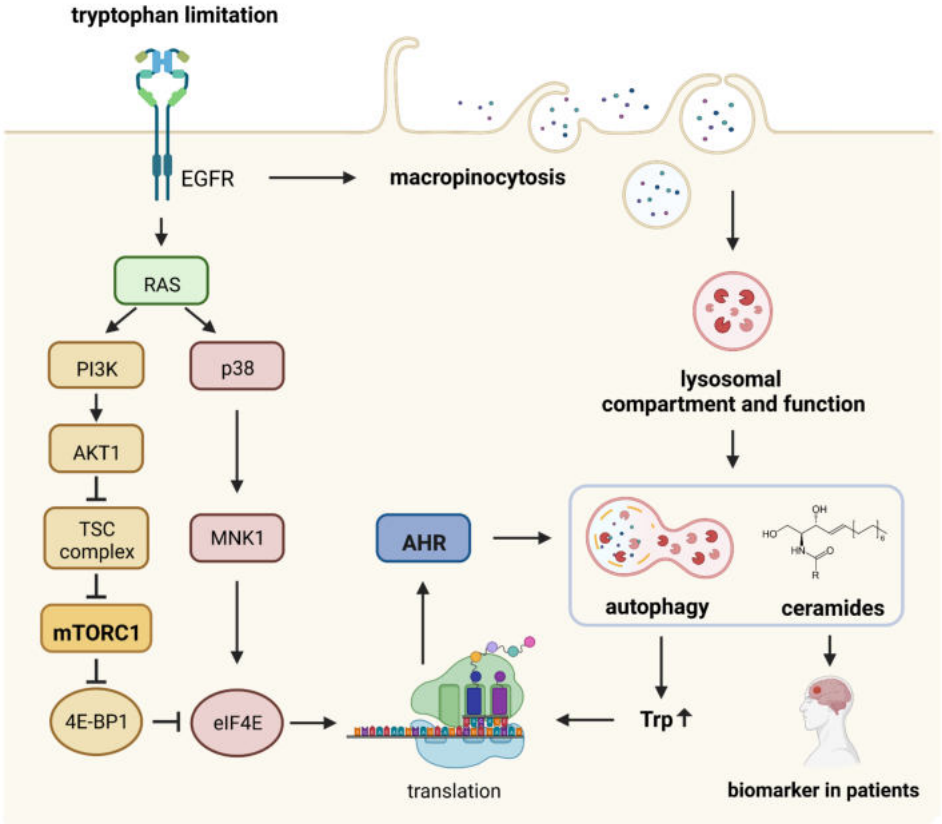
tryptophan limitation
EGFR
macropinocytosis
RAS
PI3K
p38
AKT1
TSC complex
MNK1
mTORC1
4E-BP1
eIF4E
translation
AHR
lysosomal compartment and function
autophagy
ceramides
Trp↑
biomarker in patients